





<https://doi.org/10.1038/s42003-021-02729-3>

OPEN

PIP₂-dependent coupling of voltage sensor and pore domains in K_v7.2 channel

Shashank Pant ^{1,2,3,7}, Jiaren Zhang^{4,7}, Eung Chang Kim ^{4,7}, Kin Lam^{1,2,5}, Hee Jung Chung ^{4,6,8}✉ & Emad Tajkhorshid ^{1,2,3,6,8}✉

Phosphatidylinositol-4,5-bisphosphate (PIP₂) is a signaling lipid which regulates voltage-gated K_v7/KCNQ potassium channels. Altered PIP₂ sensitivity of neuronal K_v7.2 channel is involved in *KCNQ2* epileptic encephalopathy. However, the molecular action of PIP₂ on K_v7.2 gating remains largely elusive. Here, we use molecular dynamics simulations and electrophysiology to characterize PIP₂ binding sites in a human K_v7.2 channel. In the closed state, PIP₂ localizes to the periphery of the voltage-sensing domain (VSD). In the open state, PIP₂ binds to 4 distinct interfaces formed by the cytoplasmic ends of the VSD, the gate, intracellular helices A and B and their linkers. PIP₂ binding induces bilayer-interacting conformation of helices A and B and the correlated motion of the VSD and the pore domain, whereas charge-neutralizing mutations block this coupling and reduce PIP₂ sensitivity of K_v7.2 channels by disrupting PIP₂ binding. These findings reveal the allosteric role of PIP₂ in K_v7.2 channel activation.

¹Theoretical and Computational Biophysics Group, NIH Center for Macromolecular Modeling and Bioinformatics, Beckman Institute for Advanced Science and Technology, University of Illinois at Urbana-Champaign, Urbana, IL 61801, USA. ²Department of Biochemistry, University of Illinois at Urbana-Champaign, Urbana, IL 61801, USA. ³Center for Biophysics and Quantitative Biology, University of Illinois at Urbana-Champaign, Urbana, IL 61801, USA. ⁴Department of Molecular and Integrative Physiology, University of Illinois at Urbana-Champaign, Urbana, IL 61801, USA. ⁵Department of Physics, University of Illinois at Urbana-Champaign, Urbana, IL 61801, USA. ⁶Neuroscience Program, University of Illinois at Urbana-Champaign, Urbana, IL 61801, USA. ⁷These authors contributed equally: Shashank Pant, Jiaren Zhang, Eung Chang Kim. ⁸These authors jointly supervised this work: Hee Jung Chung, Emad Tajkhorshid. ✉email: chunghj@life.illinois.edu; emad@illinois.edu

Phosphoinositides are major constituents of biological membranes and key regulators of fundamental biological processes including signal transduction, membrane trafficking, and cytoskeletal dynamics¹. Among the phosphoinositides, phosphatidylinositol-4,5-bisphosphate (PIP₂) in the plasma membrane serves as a critical cofactor for many ion channels despite its low abundance (~1% of total acidic lipids)^{2,3}. The affected channels include inward rectifier potassium (K⁺) channels⁴, voltage-gated calcium channels, transient receptor potential channels, hyperpolarization-activated cyclic nucleotide-gated channels, and voltage-gated potassium (K_v) channels^{2,5}.

PIP₂ activates all five members of the K_v channel subfamily Q (K_v7.1–K_v7.5) which control excitability of neuronal, sensory, and muscle cells^{6,7}. Encoded by *KCNQ1–KCNQ5* genes⁷, each K_v7 subunit has six transmembrane segments^{8,9}. The first four segments (S1–S4) comprise a voltage-sensing domain (VSD) with the S4 being the main voltage-sensor^{8,9}. The pore domain consists of the last two segments (S5–S6) flanking the pore loop which contains a highly conserved sequence and structure for K⁺ selectivity and permeability^{8,9}. The C-terminal intersection of four S6 segments constitutes the main gate^{9,10}. Each subunit also has a long intracellular C-terminal tail that harbors four α -helices (A–D)¹¹. Helix-A and Helix-B interact with calmodulin (CaM)¹¹, Helix-C mediates inter-subunit interaction, while Helix-D specifies the subunit assembly as a homotetramer or a heterotetramer¹¹.

Despite the common core structure, each K_v7 subunit follows a distinct, cell-specific distribution that dictates its physiological roles in different tissues^{7,8}. In the heart, K_v7.1 assembles with an auxiliary β subunit KCNE1 to produce the slow K⁺ current critical for repolarizing cardiac action potentials (APs)^{7,8}. K_v7.4 is primarily found in cochlear hair cells of the inner ear⁸. In the central nervous system, K_v7 channels are mostly heterotetramers of K_v7.2 and K_v7.3, and to a lesser extent heterotetramers of K_v7.3 and K_v7.5 and homomeric K_v7.2 channels^{12,13}. Neuronal K_v7 channels produce slowly activating and non-inactivating K⁺ current (*I_M*) that suppresses repetitive firing of APs^{12,13}, and dominant mutations in their subunits cause neonatal epilepsies including benign familial neonatal epilepsy (BFNE) and epileptic encephalopathy (EE) (rikee.org)^{14–17}. EE is a collection of epileptic syndromes accompanied by profound neurodevelopmental delay and psychomotor retardation^{18,19}.

K_v7 channels are inhibited by membrane PIP₂ depletion upon activation of G_q-coupled receptors^{2,6,13,20}. The underlying mechanism has been extensively investigated in K_v7.1³. Voltage-clamp fluorometry studies have demonstrated that depolarization can activate the VSD of K_v7.1 but fails to open the pore upon PIP₂ depletion²¹, suggesting that PIP₂ is crucial for coupling the VSD to the pore domain. In the cryo-EM structure of K_v7.1 channel in complex with KCNE3 and CaM, PIP₂ interacts with the S2–S3 and S4–S5 linkers, and this interaction may facilitate the channel opening by converting the unstructured loop between the S6 to Helix-A (pre-Helix-A) to a helix²². In addition to the S2–S3 and S4–S5 linkers and S6 as potential PIP₂ binding sites in K_v7.1²¹, *in vitro* binding studies with helices A–D of K_v7.1 have also identified basic residues in distal Helix-B that interact with PIP₂²³.

Despite the accumulating mechanistic insights into PIP₂-dependent modulation of K_v7.1³, it remains unclear whether neuronal K_v7 channels are regulated by the same PIP₂ binding residues and mechanism as K_v7.1. There are several differences in PIP₂-dependent modulation between K_v7.1 and neuronal K_v7 channels. First, PIP₂ sensitivity of K_v7.1 is regulated by KCNE1²⁴, whereas PIP₂ directly modulates neuronal K_v7 channels without auxiliary β subunits¹³. Second, previous electrophysiology studies with site-directed mutagenesis have suggested potential PIP₂ binding sites unique to K_v7.2 and K_v7.3 including the regions

between Helix-A and Helix-B (AB linker) and between Helix-B and Helix-C (BC linker)^{14,25–27}. Third, the AB linker of K_v7.2 is much longer than that of K_v7.1. Importantly, some epilepsy variants in K_v7.2 and K_v7.3 disrupt the channel sensitivity to the changes in cellular PIP₂ level^{14,25,28,29}. Therefore, detailed investigation of how PIP₂ regulates neuronal K_v7 channels can increase our understanding of their physiological function in neurons and facilitate the development of new therapeutic strategies against epilepsy.

The first step toward understanding the molecular action of PIP₂ on neuronal K_v7 channels is to identify PIP₂ binding sites. To achieve this, we employed all-atom molecular dynamics (MD) simulations. This technique has been successfully employed to provide atomic-level structural insights on lipid-protein interactions in membrane proteins with high spatiotemporal resolution^{30–34}, in close agreement with the experimental data^{30–35}. We chose to identify PIP₂ binding sites in homomeric K_v7.2 channels for several reasons. First, they produce robust K⁺ currents upon depolarization whereas homomeric K_v7.3 channels are nonfunctional^{36–39}. Second, conditional deletion of K_v7.2 but not K_v7.3 results in cortical hyperexcitability, spontaneous seizures, and high mortality in mice⁴⁰. Third, there are significantly more epilepsy mutations found in *KCNQ2* than *KCNQ3* (ClinVar Database, NCBI)^{41,42}, and current suppression of homomeric K_v7.2 channels is a common feature of EE variants of *KCNQ2*⁴³.

Here our MD simulations reveal multiple PIP₂ binding sites in homomeric K_v7.2 channels with more sites in the open state than the closed state. These sites include the S2–S3 linker, S4, S4–S5 linker, S6, pre-Helix-A, AB linker, Helix-B, and BC linker. Charge-neutralizing mutations of four PIP₂-binding residues (R214Q in the S4, K219N in the S4–S5 linker, R325Q in pre-Helix-A, and R353Q in the AB linker) disrupt PIP₂ binding to the mutated residues and decrease current densities of K_v7.2 channels. Importantly, R214Q, K219N, and R325Q mutations reduce channel sensitivity to PIP₂ depletion, with the triple R214Q/K219N/R353Q mutation inducing the largest effect. Our simulations further show that R214Q, K219N and R325Q mutations decouple the VSD activation from the pore domain of K_v7.2 channels, while the R353Q mutation blocks the PIP₂-induced increase in the propensity of helices A and B to interact with the inner leaf of the bilayer. These findings offer detailed mechanistic insights into PIP₂-dependent modulation of K_v7.2 channels.

Results

Differential PIP₂ binding in closed and open K_v7.2 channels.

To identify PIP₂ binding sites, we performed all-atom MD simulations on human K_v7.2 channels in explicit lipid bilayers composed of phosphatidylcholine and PIP₂. By adopting an integrative structural modeling approach using X-ray and cryo-EM data, we first constructed the open and closed states of K_v7.2 channels within explicit lipid bilayers (Fig. 1a). The stability of the resulting models was investigated and reported in our previous publication¹⁴. At the beginning of the lipid-binding simulations, 8 PIP₂ lipid molecules (2.2% of the total lipid in each leaflet) were distributed around the channel with their starting positions randomized in each of the three independent, 500ns-long simulation replicates (Fig. 1b, Table 1). Differential binding of PIP₂ lipids to open and closed channels was captured and presented as the PIP₂ headgroup occupancy maps extracted from the entire simulation trajectory set for each state (Fig. 1c–d). Upon binding, PIP₂ remained stably bound throughout the rest of the simulation time in all identified binding sites in both states (Fig. 1e–f).

We discover that the PIP₂ headgroup interacts with 3 distinct sites in the closed state (Fig. 1c): Site-C1 (intracellular N-terminal

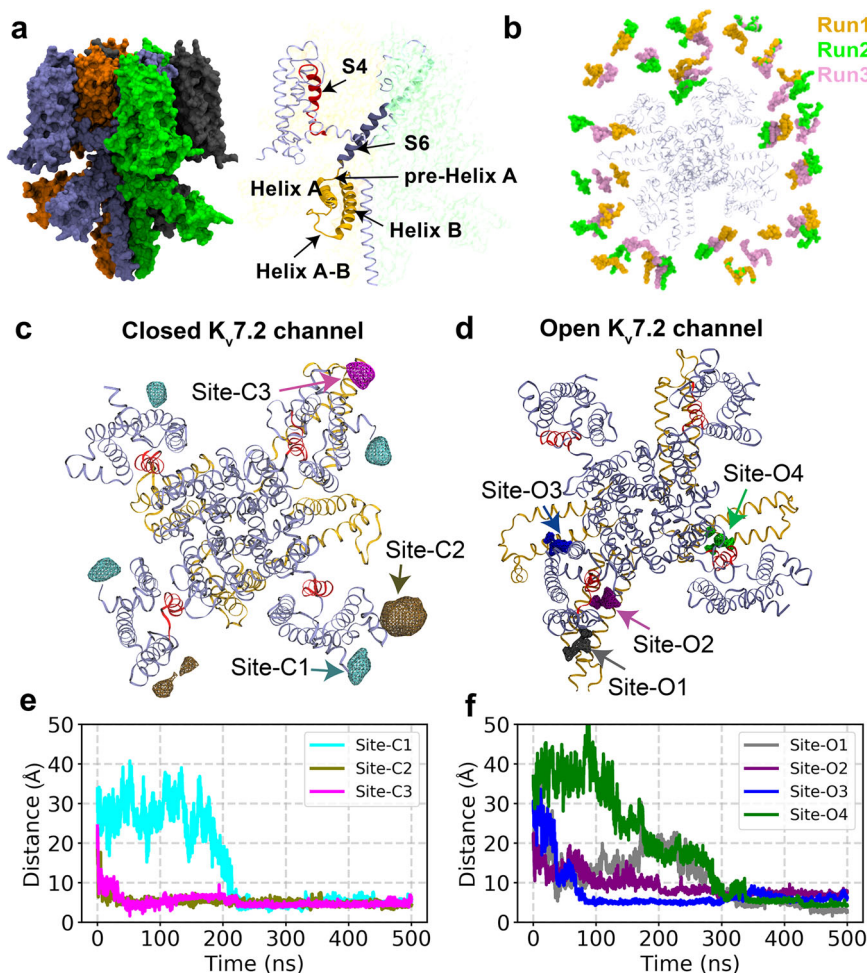


Fig. 1 Simulation design for identifying PIP₂ localization in open and closed K_v7.2 channels. **a** Left: A tetrameric K_v7.2 channel used in our simulations, where each subunit is highlighted with a different color in surface representation. Right: Detailed view of the important structural features. A tetrameric human K_v7.2 channel in a closed state was modeled from the cryo-EM structure of human K_v7.1 channel with a closed pore (PDB ID: 5VMS). For modeling the K_v7.2 channel in an open state, TMD (targeted MD) was used to drive the transition of the closed K_v7.2 state model towards the template based on the open state of K_v1.2/ K_v2.1 channel (PDB: 2R9R). **b** Top view of the simulation replicates (Runs) showing the initial placement of 8 PIP₂ molecules in both upper and lower leaflets of the lipid bilayer surrounding K_v7.2 channel in the absence of calmodulin. For each state/conformation (open or closed), 3 independent simulation replicates were performed in a tetrameric K_v7.2 channel by randomly shuffling the initial positions of PIP₂ lipids, as shown by different colors (Runs 1-3). **c-d** Volumetric maps of PIP₂ headgroup occupancy extracted collectively from the simulation trajectories are shown as wireframes overlaid on the K_v7.2 channel structure for the closed state (**c**) or the open state (**d**). We label the PIP₂ binding sites according to their proximity to the pore region. In the closed state, PIP₂ headgroups bind to Site-C1 (N-terminal tail), Site-C2 (the S2-S3 linker), and Site-C3 (at the interface formed by Helix-A, the S2-S3 linker and the AB linker). In the open conformation, PIP₂ headgroups are observed to bind Site-O1 (the interface formed by the N-terminal tail, the S2-S3 linker, distal Helix-B, and the BC linker), Site-O2 (distal Helix-B), Site-O3 (the interface formed by the S2-S3 linker, distal Helix-B, and the BC linker), and Site-O4 (the interface formed by the distal ends of the S4 and S6, the S4-S5 linker, and pre-Helix-A). **e-f** Distance between the center of mass (COM) of PIP₂ headgroup and the COM of the binding site is plotted against simulation time. Initially all PIP₂ molecules were placed at least 15 Å away from any of the binding sites captured in K_v7.2 channel structure in the closed state (**e**) and the open state (**f**). Once PIP₂ lipids bind to any of the binding sites, they remained stably bound throughout the simulation time.

tail), Site-C2 (the S2-S3 linker), and Site-C3 (the interface formed by Helix-A, the S2-S3 and AB linkers) (Fig. 1c). Notably, repeating the lipid-binding simulations on the recently solved cryo-EM structure of a closed K_v7.2 channel⁴⁴ verified the formation of the same PIP₂ binding sites (Supplementary Fig. S1). In the open state, we have identified four distinct PIP₂-binding sites, all enriched with basic residues: Site-O1 (the interface formed by the S2-S3 and AB linkers), Site-O2 (distal Helix-B), Site-O3 (the interface formed by the N-terminal tail, the S2-S3 linker, distal Helix-B, and the BC linker), and Site-O4 (the interface formed by the ends of S4 and S6, the S4-S5 linker, and pre-Helix-A) (Fig. 1d).

Although PIP₂ interact with the N-terminal tail and the S2-S3 and AB linkers in both closed and open states, there are key differences in the PIP₂ binding sites of these two states. PIP₂ headgroup occupancies at the four sites in the open channel are more focused than those at the three sites in the closed channel (Fig. 1c, d). Importantly, PIP₂ localizes to the periphery of the VSD in the closed channel, whereas PIP₂ binding spreads to a larger area in the open channel including the cytoplasmic ends of the VSD and S6, pre-Helix-A, distal Helix-B, and the BC linker (Fig. 1c, d), suggesting that the opening of K_v7.2 channels involves PIP₂ interaction with VSD, the gate, and intracellular helices.

Table 1 Details of the systems and the simulations performed.

Channel	Lipid composition	Simulated replicas	Time per replica (ns)
WT (open)	POPC + PIP ₂ (2.2%)	3	500
WT (closed)	POPC + PIP ₂ (2.2%)	3	500
WT (closed) (7CR3)	POPC + PIP ₂ (2.2%)	3	500
WT (open)	POPC	1	500
K219N (open)	POPC + PIP ₂ (2.2%)	3	500
R325Q (open)	POPC + PIP ₂ (2.2%)	3	500
R214Q (open)	POPC + PIP ₂ (2.2%)	3	500
R353Q (open)	POPC + PIP ₂ (2.2%)	3	500

POPC: 1-palmitoyl-2-oleoyl-sn-glycero-3-phosphatidylcholine
 PIP₂: 1-palmitoyl-2-oleoyl-sn-glycero-3-phosphatidylinositol 4,5-bisphosphate

Characterizing specific lipid-protein interactions in K_v7.2 channels.

To map PIP₂-binding sites, we analyzed lipid-protein interactions during the last 200 ns of MD trajectories by quantifying the contact probability between each moiety of the PIP₂ headgroup and the PIP₂-binding residues. In the closed channel, Site-C1 is formed by a cluster of basic residues (K76, R87, and R89) in the intracellular N-terminal tail. R87 and R89 exclusively interact with P5-phosphate, whereas K76 establishes contacts with all the hydroxyl and phosphate groups on the inositol ring in PIP₂ (Supplementary Fig. S2a, d). In Site-C2, a cluster of basic residues in the S2-S3 linker (R153, R158, and K162) coordinate PIP₂. R153 and K162 show high contact probabilities to P4-phosphate and P5-phosphate, whereas R158 interacts with all groups in PIP₂ (Supplementary Fig. S2b, e). Site-C3 is formed by R155 in the S2-S3 linker, Y347 in Helix-A, and R353 in the AB linker. R155 has high contact probabilities for P5-phosphate and the hydroxyl group at position 6 of the inositol ring, whereas R353 interacts preferentially with P4- and P5-phosphates (Supplementary Fig. S2c, f).

In the open channel, Site-O1 is formed by residues in the S2-S3 linker (K162 and R165) and the AB linker (F346, Y347, and R353) (Fig. 2a, b). All the three basic residues in this site show high contact probabilities for P5-phosphate on PIP₂ headgroup (Fig. 2a). In Site-O2, a cluster of basic residues in distal Helix-B (K552, R553, and K554) coordinate PIP₂ (Fig. 2b, f). K552 and R553 primarily bind to P5-phosphate, while K554 interacts with P4- and P5-phosphates and hydroxyl group at position 3 of the inositol ring (Fig. 2b). Site-O3 is formed by residues in the intracellular N-terminal tail (R87), the S2-S3 linker (R153, Y154, and K166), distal Helix-B (R553), and the BC linker (R560) (Fig. 2c, g). Y154 and K166 predominantly interact with P4-phosphate, whereas the other basic residues bind to P5-phosphate. In Site-O4, PIP₂ interacts with R214 at the end of S4, K219 in the S4-S5 linker, K319 and Q323 in distal end of S6, and R325 in pre-Helix-A (Fig. 2d, h). Most of these residues, except K319, show high contact probabilities for P5-phosphate in PIP₂.

Overall, PIP₂ binds to many more basic residues in the open state than the closed state. However, both states share 4 common PIP₂ binding residues including R87 at the N-terminal tail, R153 and K162 in the S2-S3 linker, and R353 in the AB linker. Interestingly, the simulation trajectories (Supplementary Movies 1–3) show that R353 comes in contact with PIP₂ first after which the lipid forms contacts with other residues in Site-O1, suggesting that R353 might act as an initial anchor point of PIP₂ in Site-O1.

Charge-neutralizing mutations of potential PIP₂ binding residues disrupt voltage-dependent activation of K_v7.2 channels. PIP₂ is required for activation of all K_v7 channels³. To test

the functional impact of PIP₂ binding sites identified by our MD simulations, we introduced charge-neutralizing mutations in select residues that had high contact probability to PIP₂ headgroups. In Site-O4, we introduced R214Q in the distal S4, K219N in the S4-S5 linker, and R325Q in pre-Helix-A (Fig. 3a–i). Since MD simulations identified R353 as an initial anchoring point for PIP₂ in Site-O1, we also made R353Q in the AB linker (Fig. 3j–l). To test if charge-neutralizing mutations disrupt PIP₂ binding to mutated basic residues, we performed 500-ns MD simulations after introducing each mutation in the PIP₂-bound conformation of wild-type (WT) channels and monitored the distance between the PIP₂ headgroup and the mutated residues.

Upon introducing R214Q, we observed that the bound PIP₂ dissociated from the mutated residue and Site-O4 and diffused to basic residues in distal Helix-B in 2 out of 3 simulations (Fig. 3a–c). The introduction of K219N or R325Q resulted in dissociation of PIP₂ from the mutated residue in all simulations (Fig. 3d–i). Compared to the WT channel (Fig. 2d, h), these mutations also decreased PIP₂ binding to K319 and Q323 but not to other basic residues in Site-O4 (Fig. 3e–f, h–i). Introduction of R353Q resulted in dissociation of PIP₂ from the mutated residue in all simulations, although PIP₂ remained bound to K162 and R165 in Site-O1 (Fig. 3j–l).

To test if these mutations affect voltage-gated activation of K_v7.2 channels, we performed whole cell patch clamp recording in CHO hm1 cells^{14,25,45}, which display depolarized resting membrane potential (V_m) due to a low level of endogenous K⁺ channels^{45,46}. Application of depolarizing voltage steps from -100 to $+20$ mV in cells transfected with GFP and WT K_v7.2 produced a slowly activating outward K⁺ current with peak current density of 26.5 ± 1.4 pA/pF at $+20$ mV (Fig. 4a–c, Supplementary Fig. S3). Current activation was sigmoidal, and full activation was reached from 0 mV step with half-maximal current activation potential ($V_{1/2}$) of -30.5 ± 0.5 mV (Fig. 4a–d, Table 2). Due to this increase in outward K⁺ currents, these cells also displayed hyperpolarized V_m compared to cells transfected with GFP alone (Supplementary Table S1).

Compared to WT channels, K_v7.2-K219N channels produced K⁺ currents with significantly smaller peak current density (8.2 ± 1.6 pA/pF at $+20$ mV), a large depolarizing shift in $V_{1/2}$ (-13.7 ± 1.7 mV), and a slower activation kinetic (Fig. 4a–e, Table 2). The R325Q mutation significantly reduced peak current density by $\sim 90\%$ (3.5 ± 0.4 pA/pF at $+20$ mV) (Fig. 4a–c). At -20 to $+20$ mV, the R325Q-transfected cells produced currents that were larger than those in cells transfected with GFP alone (Supplementary Fig. S3g), suggesting that K_v7.2-R325Q channels are functional. The peak current densities of K_v7.2-R214Q and K_v7.2-R353Q channels were also decreased by $\sim 30\%$, but their voltage dependence and activation time constant were unaffected (Fig. 4a–e, Supplementary Figs. S3–S4). Similar surface expressions were observed for WT and all tested mutants except for K_v7.2-R214Q, which displayed lower surface expression than the WT ($61.8 \pm 11.0\%$ of WT, Supplementary Fig. S5). The surface/total protein ratio of all tested mutants did not differ from WT K_v7.2 (Supplementary Fig. S5e), suggesting that none of the mutations affected the proportion of K_v7.2 to express on the plasma membrane.

Charge-neutralizing mutations of potential PIP₂ binding residues alter PIP₂ sensitivity of K_v7.2 channels.

To test if charge-neutralizing mutations alter gating modulation of K_v7 channels by PIP₂, we increased cellular PIP₂ level by co-transfecting phosphatidylinositol-4-phosphate 5-kinase (PIP5K) which converts phosphatidylinositol 4-phosphate to PIP₂⁴⁷. Since the endogenous membrane level of PIP₂ is not enough to saturate K_v7 channel

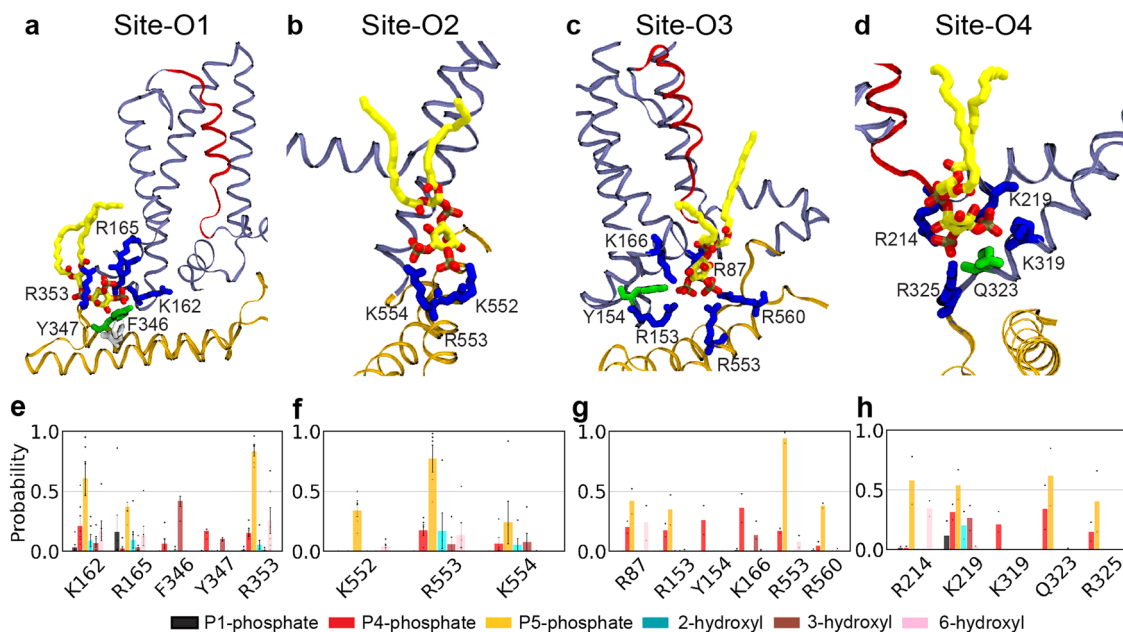


Fig. 2 PIP₂ coordination in 4 binding sites captured in the modeled structure of the open K_v7.2 channel. **a–d** PIP₂ coordination in Site-O1 (**a**), Site-O2 (**b**), Site-O3 (**c**), and Site-O4 (**d**). K_v7.2 protein is shown in ribbon representation with S4 in red, helices A and B in brown, and the rest of the protein in ice blue. A PIP₂ lipid (carbon atoms in yellow, oxygen in red, and phosphorus atoms in tan) and the residues of the binding pocket at each site at the end of simulations are shown in sticks (basic residues in blue, polar in green, acidic in red, and hydrophobic in white). **e–h** The contact probability for each chemical moiety of PIP₂ headgroup with the key residues in the binding Site-O1 (**e**), Site-O2 (**f**), Site-O3 (**g**), and Site-O4 (**h**). The chemical moieties of PIP₂ headgroup include P1-phosphate (black), P4-phosphate (red), P5-phosphate (orange), 2-hydroxyl (cyan), 3-hydroxyl (brown), and 6-hydroxyl (pink) group of the inositol ring. A heavy-atom distance cutoff of 4 Å was used to define a contact between a protein residue and a phosphate group of PIP₂, whereas a 3.5 Å cutoff was used to define a contact between a residue and a hydroxyl group of PIP₂. Analysis of the contact probabilities was performed over the last 200 ns of the simulation trajectories. The number of PIP₂ interacting events: Site-O1 ($n = 6$), Site-O2 ($n = 5$), Site-O3 ($n = 2$), and Site-O4 ($n = 2$). Data represent mean \pm SEM for analysis of each monomer in 3 independent trajectories.

activation²⁴, enhancing cellular PIP₂ level by PIP5K expression is shown to increase single-channel open probability⁴⁸ and whole-cell current densities of K_v7.2 channels^{14,28}. Consistent with previous reports^{14,28,48}, PIP5K expression significantly increased peak K_v7.2 current density by 4.4 ± 0.2 -fold (118.7 ± 4.7 pA/pF) with a hyperpolarizing shift in their voltage dependence and a faster activation kinetic (Fig. 4a–e, Supplementary Figs. S3–S4).

In contrast, the R325Q mutation abolished the PIP5K-induced current potentiation (Fig. 4a–c, Supplementary Figs. S3–S4). In the presence of PIP5K, K_v7.2 channels containing R214Q, K219N or R353Q mutations produced significantly less outward K⁺ currents compared to WT channels (K_v7.2-R214Q: 79.3 ± 6.8 pA/pF; K_v7.2-K219N: 51.1 ± 3.9 pA/pF; K_v7.2-R353Q: 70.3 ± 3.0 pA/pF) (Fig. 4a–e, Supplementary Figs. S3–S4, Table 2). However, the fold increases in their PIP5K-induced current potentiation were comparable to the WT channels (4.7 ± 0.4 fold for R214Q, 6.2 ± 0.5 fold for K219N, 4.0 ± 0.2 fold for R353Q) (Fig. 4a–e, Supplementary Figs. S3–S4, Table 2), suggesting that the charge-neutralizing mutation of a single residue may not be sufficient to fully dissociate PIP₂ from Site-O4 and Site-O1 (Fig. 3b,e,h,k).

Therefore, we next generated the R214Q/K219N double mutant (DM) and the R214Q/K219N/R353Q triple mutant (TM). Compared to K_v7.2-WT channels, both DM and TM channels displayed smaller peak current densities (DM = 12.5 ± 0.6 pA/pF, TM = 12.9 ± 1.3 pA/pF) and activated at more depolarized voltages with slower activation kinetics (Fig. 4a–e, Supplementary Figs. S3–S4, Table 2). PIP5K co-expression increased the peak current density of DM channels by 4.3 ± 0.3 -fold (53.5 ± 4.1 pA/pF) but that of TM channels only by 2.1 ± 0.2 -fold (27.5 ± 2.7 pA/pF) (Fig. 4a–e, Supplementary Figs. S3–S4, Table 2), indicating that the triple mutation decreased the channel sensitivity to PIP₂ enhancement.

To further investigate PIP₂ sensitivity of mutant channels, we examined current decay upon membrane PIP₂ depletion. To achieve this, we coexpressed *Danio rerio* voltage-sensitive phosphatase (Dr-VSP)¹⁴. Upon activation of Dr-VSP, K⁺ currents through WT channels reached a maximal decay of at +100 mV (0.52 ± 0.02 , Fig. 5a–c). K_v7.2-R353Q channels displayed larger current decays at +40 and +60 mV, but showed similar decays to WT channels at +100 mV (Fig. 5a–c). In contrast, the VSP-induced current decays of R214Q and K219N channels were smaller than WT channels and were minimal in K_v7.2-R325Q, DM, and TM channels (Fig. 5a–c), indicating these mutants have decreased sensitivity to PIP₂ depletion.

PIP₂-mediated correlated motions of the VSD and the pore domain.

Voltage-dependent conformational changes of the VSD and the pore domain are critical for the gating of K_v channels⁴⁹. To examine PIP₂-mediated allosteric interactions, we investigated the communities formed in the WT and mutant channels by employing dynamic network analysis and Pearson correlation. These communities correspond to sets of residues that move in a correlated manner during the MD simulations and thus represent strongly connected regions. We detected the presence of a pronounced community connecting the end of S4, the S4-S5 linker, S6, and pre-Helix-A in WT channels (Fig. 6a). The thickness of the edges connecting the amino acids corresponds to the strength of the correlation between them. All mutant channels show thinner edges within this community (Fig. 6b–d), indicating weaker correlated motions in this area compared to WT channels. Interestingly, we also detected the emergence of additional (sub) communities in all the studied mutants (Fig. 6b–d), in line with the described weaker interactions in this region. The presence of

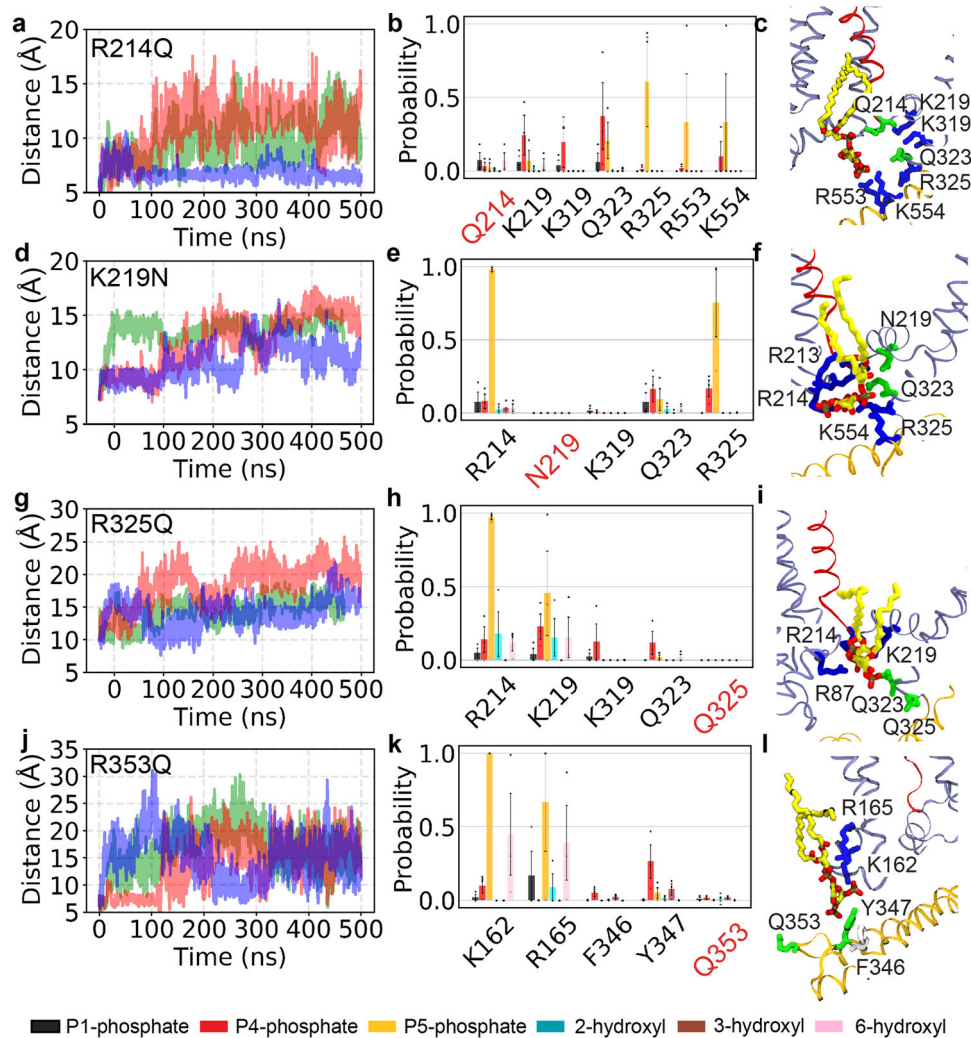


Fig. 3 Charge-neutralizing mutations disrupt PIP₂ binding to the mutated residues in the open K_v7.2 channel. **a, d, g, j** Time evolution of the distance between the COM of PIP₂ headgroup and the COM of the mutated residue upon introducing mutations including R214Q (**a**), K219N (**d**), R325Q (**g**), and R353Q (**j**) in PIP₂-bound K_v7.2 channel in an open state from three independent simulations (different colors). Introduction of these mutations resulted in the dissociation of bound PIP₂ lipid, as indicated by the distance increase. **b, e, h, k** The contact probability for each chemical moiety of PIP₂ headgroup with the key residues in open K_v7.2 channels containing R214Q (**b**), K219N (**e**), R325Q (**h**), and R353Q (**k**). The chemical moieties of PIP₂ headgroup include P1-phosphate (black), P4-phosphate (red), P5-phosphate (orange), 2-hydroxyl (cyan), 3-hydroxyl (brown), and 6-hydroxyl (pink) group of the inositol ring. A heavy-atom distance cutoff of 4 Å was used to define a contact between a residue and a phosphate group of PIP₂, whereas a 3.5 Å cutoff was used to define a contact between a residue and a hydroxyl group of PIP₂. Analysis of the contact probabilities was performed over the last 200 ns of the simulation trajectories. The number of PIP₂ interacting events: R214Q ($n = 3$), K219N ($n = 3$), R325Q ($n = 3$), and R353Q ($n = 3$). Data represent mean \pm SEM for 3 independent trajectories. **c, f, i, l** PIP₂ coordination in Site-O4 of K_v7.2-R214Q (**c**), K_v7.2-K219N (**f**), and K_v7.2-R325Q (**i**) and in Site-O1 of K_v7.2-R353Q (**l**) channel at the end of the respective simulations. The protein is shown in ribbon representation with the S4 in red, helices A and B in brown, and the rest of the protein in ice blue. A PIP₂ lipid (carbon atoms in yellow, oxygen in red, and phosphorus in tan) and the residues of the binding pocket at each site are shown in sticks (basic residues in blue, polar in green, acidic in red, and hydrophobic in white).

disconnected communities suggests uncorrelated dynamics of this region (Site-O4) after decreased PIP₂ binding (Fig. 3). These data suggest that R214Q, K219N, and R325Q mutations disrupt the correlated motions of the VSD and the S6 gate in the pore domain of K_v7.2.

PIP₂-dependent conformational change of helices A and B. The cryo-EM structure of K_v7.1/KCNE3 in complex with CaM suggests that PIP₂ induces a conformational change in the cytoplasmic domain that may facilitate the opening of K_v7.1 channels²². To test the conformational impact of PIP₂ on K_v7.2 channels, we compared the dynamics of the open channel in PIP₂-containing lipid bilayers with a control simulation performed in the absence of PIP₂ lipids.

The most significant PIP₂-induced conformational change was observed in the cytoplasmic helices A and B (Fig. 7a–b). The effect was quantified by calculating the orientation of the helical pair with respect to the membrane normal (Fig. 7c). In a PIP₂-free lipid bilayer, these helices fluctuate around their initial position ($\theta = 83.8 \pm 13.2^\circ$) and remain in a largely solvent-exposed conformation (Fig. 7a,c). In the presence of PIP₂, the helices adopt a conformation where they interact directly with the lipid bilayer ($\theta = 95.5 \pm 3.7^\circ$) (Fig. 7b–c). This large-scale conformational change also forms a pathway for PIP₂ to move along Helix-B and ultimately bind to Site-O4 (Fig. 7d, Supplementary Movie 4). Since R353 in the AB linker acts as an initial anchor point for PIP₂ binding (Supplementary Movies 1–3), we next tested if a charge-neutralizing

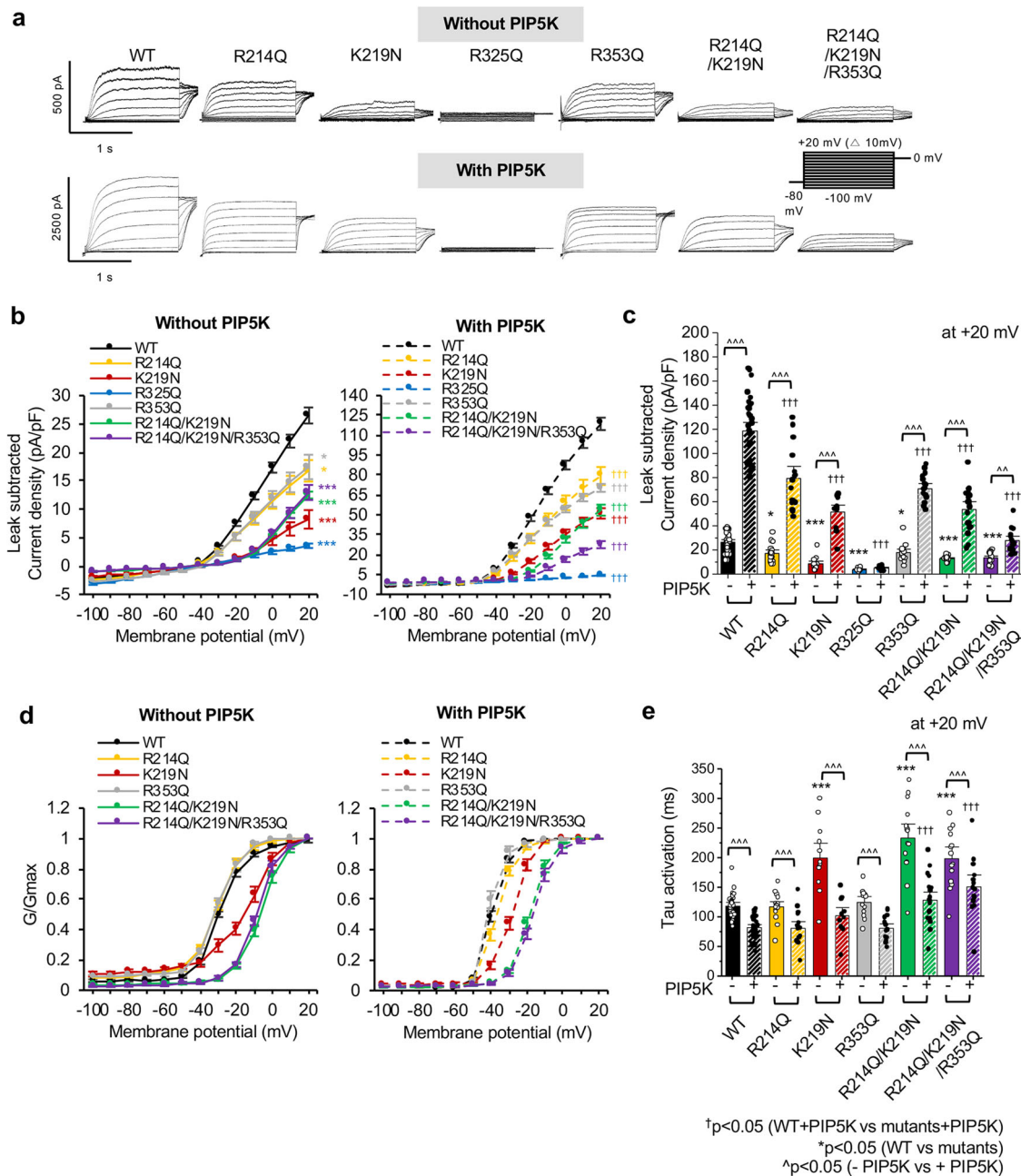


Fig. 4 Charge-neutralizing mutations of potential PIP₂ binding residues decrease voltage- and PIP₂-dependent activation of homomeric K_v7.2 channels. Whole cell voltage clamp recordings of macroscopic K⁺ currents through K_v7.2 WT or mutant channels were performed in CHO hm1 cells cotransfected with GFP and PIP5K. The DNA plasmid ratio was 0.2:0.45:0.45 (GFP: K_v7.2 WT or mutant: PIP5K). Cells were held at -80 mV. K⁺ currents were evoked by depolarizing voltage steps for 1.5 s from -100 mV to +20 mV in 10-mV increments, followed by a step to 0 mV for 300 ms. **a** Representative traces after subtraction of leak currents. Leak current was defined as non-voltage-dependent current from GFP-transfected cells. Note different Y-axis scales for systems with and without PIP5K. **b** Average peak current densities (pA/pF) of K_v7.2 WT or mutant channels with or without PIP5K coexpression at all voltage steps. **c** Average peak current densities of WT or mutant K_v7.2 channels at +20 mV. p values are computed from one-way ANOVA post-hoc Fisher’s test. **d** Normalized conductance (G/G_{max}) at all voltage steps. **e** Average activation constant (τ) at +20 mV. The number of GFP-positive cells that were recorded without PIP5K coexpression: K_v7.2 WT (n = 31), R214Q (n = 16), K219N (n = 12), R325Q (n = 11), R353Q (n = 13), R214Q/ K219N (n = 15), R214Q/K219N/R353Q (n = 14). The number of GFP-cotransfected cells that were recorded with PIP5K: K_v7.2 WT (n = 33), R214Q (n = 15), K219N (n = 12), R325Q (n = 11), R353Q (n = 16), R214Q/ K219N (n = 19) or R214Q/K219N/R353Q (n = 14). The source data for Fig. 4b and Fig. 4d are available in Figshare⁹³. Data represent the mean ± SEM. One-way ANOVA with post-hoc Fisher’s multiple comparison test was used. GFP + selected variant: *p < 0.05 for K_v7.2 WT vs. mutant (**p < 0.01, ***p < 0.005); †p < 0.05 for K_v7.2 WT + PIP5K vs. mutants + PIP5K (††p < 0.01, †††p < 0.005); ^p < 0.05 for the difference between -PIP5K and +PIP5K within the same transfection (^^p < 0.01, ^^p < 0.005).

Table 2 Biophysical properties of K_v7.2 homomers in CHO hm1 cells co-transfected with GFP and PIP5K.

Transfection	<i>n</i>	Leak subtracted <i>I</i> at +20 mV (pA)	G/G _{max} V _{1/2} (mV)	G/G _{max} k(mV/e fold)
GFP	12	27.3 ± 4.0*	-65.8 ± 9.2*	0.7 ± 0.2*
GFP + WT	31	567.7 ± 43.3	-30.5 ± 0.5	5.9 ± 0.7
GFP + R214Q	16	299.6 ± 35.5*	-31.4 ± 0.5	4.3 ± 0.4*
GFP + K219N	12	150.4 ± 32.4*	-13.7 ± 1.7*	6.5 ± 0.7
GFP + R325Q	11	63.9 ± 7.5*	-65.1 ± 3.6*	1.2 ± 0.4*
GFP + R353Q	13	310.2 ± 39.9*	-31.7 ± 1.1	5.0 ± 1.1
GFP + R214Q/K219N	15	284.1 ± 19.5*	-9.7 ± 0.6*	5.6 ± 0.4*
GFP + R214Q/K219N/R353Q	14	312.4 ± 38.5*	-9.8 ± 1.0*	5.5 ± 0.6
GFP + WT + PIP5K	33	2164.0 ± 92.4 [†]	-40.3 ± 0.6 [^]	2.3 ± 0.3 [^]
GFP + R214Q + PIP5K	15	1500.8 ± 138.3 [†]	-38.7 ± 0.7 [^]	2.2 ± 0.4 [^]
GFP + K219N + PIP5K	12	981.9 ± 92.9 [†]	-29.4 ± 0.8 [^]	3.2 ± 0.6 [^]
GFP + R325Q + PIP5K	11	75.0 ± 9.2 [†]	-33.3 ± 3.0 [^]	8.5 ± 1.4 [^]
GFP + R353Q + PIP5K	16	1373.5 ± 79.5 [†]	-42.4 ± 1.2 [^]	1.2 ± 0.3 [^]
GFP + R214Q/K219N + PIP5K	19	997.7 ± 70.4 [†]	-20.5 ± 0.9 [^]	3.8 ± 0.6 [^]
GFP + R214Q/K219N/R353Q + PIP5K	14	492.2 ± 48.4 [†]	-20.8 ± 1.2 [^]	4.3 ± 0.9 [^]

n number, NA not applicable, Leak subtracted peak current (*I*) measured at +20 mV, V_{1/2} half-activation potential, *k* the slope factor, τ activation time constant measured at +20 mV. All values are calculated from leak subtracted current. V_{1/2} and *k* are calculated from normalized conductance G/G_{max}. Mean ± SEM (GFP + selected variant): **p* < 0.05 for K_v7.2 WT vs. mutant; [†]*p* < 0.05 for K_v7.2 WT + PIP5K vs. mutants + PIP5K; [^]*p* < 0.05 for the difference between -PIP5K and +PIP5K within the same transfection. The source data for Table 2 is available in Figshare⁹³.

mutation at this residue (R353Q) affects the PIP₂-induced conformational change. We found that the R353Q mutation moves the helices back toward a more solvent-exposed conformation ($\theta = 86.7 \pm 1.9^\circ$) (Fig. 7c).

Discussion

Neuronal K_v7 channels are known as the “M-channels” due to their inhibition by the activation of M1 and M3 muscarinic acetylcholine receptors¹³. PIP₂ hydrolysis underlies current inhibition of M-channels, bringing attention to K_v7-PIP₂ interaction^{6,20}. Increasing the PIP₂ level enhances current density and the open probability of K_v7.2 channels and induces a hyperpolarized shift in their voltage-dependence^{6,14,25,28,48}. However, the detailed mechanism underlying PIP₂-dependent regulation of neuronal K_v7 channel remains unclear. In this study, we address this knowledge gap by identifying PIP₂ interaction sites in both open and closed K_v7.2 channels.

Our all-atom MD simulations have revealed PIP₂ localization to 3 sites at the periphery of the VSD in the closed K_v7.2 channel, whereas PIP₂ binds to 4 distinct sites at the VSD, the pore domain, and intracellular helices in the open channel (Fig. 1, Supplementary Figs. S1–S2). The common PIP₂ binding domains in both open and closed channels are the intracellular N-terminal tail, the S2-S3 and AB linkers. Importantly, PIP₂ binding in the open channel is coordinated by multiple basic residues from different functional domains of K_v7.2.

Our identification of the S2-S3 and S4-S5 linkers as PIP₂ binding domains is consistent with a previous simulation study reported by Zhang et al.⁵⁰. However, our study has identified many more PIP₂ binding regions in K_v7.2 channel compared to Zhang et al. These include the intracellular N-terminal tail, the distal ends of the S4 and S6 as well as pre-Helix-A, Helix-A, the AB linker, Helix-B, and the BC linker in the intracellular C-terminal tail. The difference could be attributed to structural templates used in each study. Our homology model of K_v7.2 was based on the cryo-EM structure of K_v7.1 containing cytoplasmic helices A-C and a part of intracellular N-terminal tail¹⁰. In contrast, Zhang et al modeled the K_v7.2 transmembrane domains only (residues 95–337) based on the crystal structures of K_v1.2 and an activated bacterial K⁺ channel KcsA⁵⁰. In the following sections, we discuss the functional implications of the additional PIP₂ binding sites, which we have identified in this study.

To the best of our knowledge, our MD simulations have identified a novel PIP₂-interacting interface in the open K_v7.2 channel, Site-O4, which is comprised of the distal ends of S4 and S6, the S4-S5 linker, and pre-Helix-A. We show that R325 in pre-Helix-A interacts with PIP₂ (Fig. 2), and its charge-neutralizing mutation, R325Q, abolishes this interaction (Fig. 3), basal current, and the sensitivity to PIP₂ (Figs. 4–5). Severe reduction in current expression and PIP₂ sensitivity has also been reported in K_v7.2 channels containing recurrent EE variant R325G²⁸ which causes drug-resistant seizures, neurodevelopmental delay, and intellectual disability^{18,51}. The R325 is the first residue in a “RQKH” motif conserved in all K_v7 subunits^{3,22,28}. This motif in K_v7.1 undergoes a PIP₂-induced conformational change from an unstructured loop to a helix²², further supporting that PIP₂ binding to R325 is involved in activation of K_v7.2 channels.

In Site-O4, PIP₂ also interacts with R214 in distal S4 and K219 in the S4-S5 linker in the open channel (Figs. 1 and 2). Although the S4-S5 linker was previously reported to mediate PIP₂ modulation of K_v7.1-K_v7.3^{3,21,50,52}, to the best of our knowledge, the identification of R214 as a PIP₂ binding site in K_v7.2 is a novel finding. R214 is also the target of two epilepsy mutations^{53–55}, supporting its functional importance. Although the charge-neutralizing mutations R214Q and K219N reduce PIP₂ interactions with the mutated residues (Fig. 3), their reduced sensitivity to PIP₂ depletion (Fig. 5) suggests increased PIP₂ affinity to other residues of the channel. K219N, but not R214Q, induces a depolarizing shift in voltage dependence (Fig. 4) similar to R243A and K248A in the corresponding residue in K_v7.3^{27,52}. However, the double R214Q/K219N mutation further shifts the activation curve to a depolarized potential and induces less sensitivity to PIP₂ depletion compared to single mutants (Figs. 4–5), demonstrating the synergistic effects. These findings suggest that PIP₂ interaction with both the distal S4 and the S4-S5 linker is needed for robust voltage-dependent activation of K_v7.2 channels.

Previous studies proposed the role of PIP₂ in coupling of the VSD activation to pore opening in K_v7.1 and K_v7.3^{10,21,22,52,56}. In K_v7.2 channels, we observe that PIP₂ binding to Site-O4 forms an allosteric network of interactions, leading to a correlated motion of the main voltage sensor S4, the S4-S5 linker, the gate S6, and pre-Helix-A (Fig. 6), suggestive of the coupling of the VSD to the pore domain. Charge neutralizing mutations (R214Q, K219N, or R325Q) induce PIP₂ dissociation from the mutated residues (Fig. 3) and disrupt the coordinated movements of the

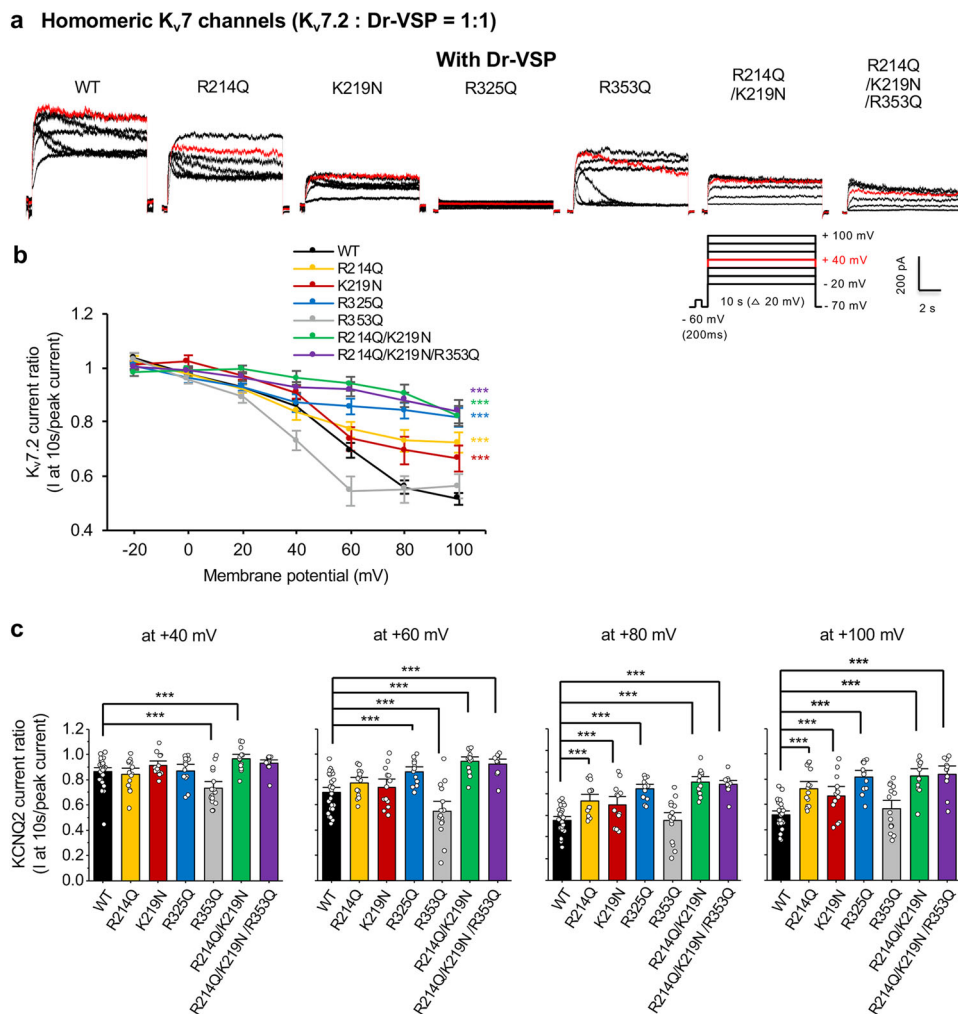


Fig. 5 Charge-neutralizing mutations of potential PIP_2 binding residues alter $K_v7.2$ current response to Dr-VSP activation. **a** Representative current traces showing Dr-VSP-mediated $K_v7.2$ current decay in CHO hm1 cells co-expressing Dr-VSP and $K_v7.2$ WT or mutants from -20 mV to $+100$ mV. CHO cells were held at -70 mV, and a brief voltage step to -60 mV was applied to calculate the linear leak. 10 s step depolarizations were applied in 20 -mV steps from -20 to $+100$ mV with 2 min inter-step intervals to allow PIP_2 regeneration. Red trace shows current decay curve when cells were held at $+40$ mV. **b** Ratio of current decay in $K_v7.2$ WT or mutant channels at each voltage step. **c** $K_v7.2$ current decay ratio at $+40$ mV, $+60$ mV, $+80$ mV and $+100$ mV. The number of cotransfected cells that were recorded with EGFP-tagged Dr-VSP: $K_v7.2$ WT ($n = 27$), R214Q ($n = 14$), K219N ($n = 13$), R325Q ($n = 12$), R353Q ($n = 15$), R214Q/ K219N ($n = 13$) or R214Q/K219N/R353Q ($n = 11$). The source data for Fig. 5b is available in Figshare⁹³. Data represent the mean \pm SEM. One-way ANOVA Fisher's test results are shown ($*p < 0.05$, $**p < 0.01$ and $***p < 0.005$).

VSD and the pore domain (Fig. 6), indicative of their decoupling. To the best of our knowledge, this is the first study to provide an atomic-level structural basis for the allosteric role of PIP_2 in voltage-dependent activation of neuronal $K_v7.2$ channels.

Our MD simulations have identified Site-O2 comprised of the K552-R553-K554 motif in Helix-B and with R560 in the BC linker as a PIP_2 binding site in the open state (Fig. 2). We have previously shown that current potentiation induced by increasing PIP_2 level is abolished by EE mutations K552T, R553L, and R560W^{14,25} but enhanced by K554N²⁵, highlighting the role of these basic residues in PIP_2 modulation of $K_v7.2$ channels^{14,25}. The corresponding basic residues in Helix-B of $K_v7.1$ bind to PIP_2 in vitro²³ but those in $K_v7.3$ do not affect its sensitivity to PIP_2 depletion²⁷, suggesting the subunit-specific difference of Helix-B in mediating PIP_2 binding.

Our simulations also demonstrate that PIP_2 interacts with Site-O1 formed by F346, Y347, and R353 at the beginning of the AB linker and with K162 and R165 in the S2-S3 linker (Fig. 2). Due to the presence of a lysine residue (K162) and two aromatic residues (F346 and Y347), this site fulfills the requirement for a

canonical PIP_2 binding site⁵⁷. Consistent with the conserved sequence of the S2-S3 linker among K_v7 subunits³, PIP_2 binding to this linker has also been reported in $K_v7.1$ ^{3,21,22,58} and $K_v7.3$ ^{27,52}, suggesting the role of this linker in PIP_2 modulation of K_v7 channels.

Although a “cationic cluster” (K452/R459/K461) in the distal region of the AB linker is implicated in PIP_2 modulation of $K_v7.2$ current²⁶, the charge-neutralizing mutation of R353 in the proximal region of this linker reduces basal current expression of $K_v7.2$ channels and increases current inhibition upon PIP_2 depletion, suggestive of decreased PIP_2 affinity (Figs. 4–5). Combination of R353Q with R214Q and K219N in Site-O4 further reduces basal current and the PIP_5K -induced current enhancement (Fig. 4), suggesting that R353 modulates $K_v7.2$ channels by coordinating PIP_2 binding with other residues. Indeed, R353 serves as an initial anchor point for PIP_2 binding to Site-O1 and Site-O4 (Supplementary Movies 1–4). Furthermore, PIP_2 induces the conformational change of helices A and B from the largely solvent-exposed conformation to a bilayer-interacting conformation, whereas the R353Q mutation attenuates this effect

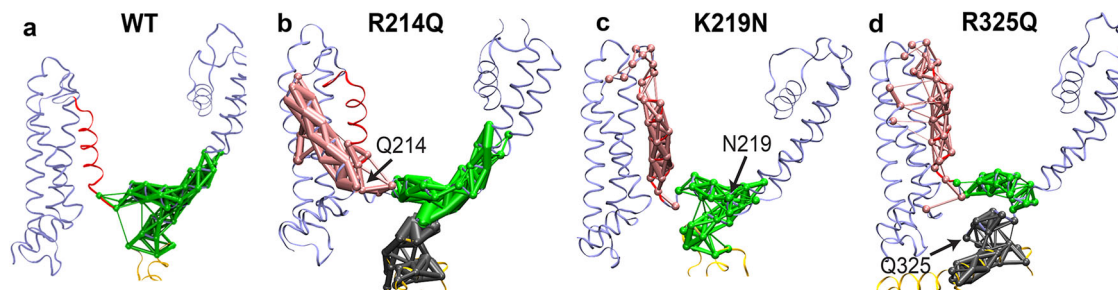


Fig. 6 Charge-neutralizing mutations of potential PIP₂ binding residues in Site-O4 disrupt the correlated motions of the VSD and the S6 gate of K_v7.2 channels. Network-based community analysis in WT (**a**) and mutant K_v7.2 channels containing R214Q (**b**), K219N (**c**), and R325Q (**d**) mutations in Site-O4. A community represents a set of residues that move in a correlated manner during the MD simulations. The thickness of the edges between the amino acids within each community corresponds to the strength of correlation between them. The network analysis was performed after combining all 3 independent simulation trajectories. **a** Binding of PIP₂ at Site-O4 in the WT channel results in correlated motions of the VSD (the S4 and the S4-S5 linker) and the gate S6, highlighted by a single community in green. **b** Introduction of the R214Q mutation leads to uncorrelated motions of the VSD and the gate, highlighted by 3 separate communities colored in pink, green, and gray. **c** Introduction of the K219N mutation leads to uncorrelated motions of the VSD and the gate, highlighted by the smaller community in green and the emergence of an additional community colored in pink. **d** K_v7.2-R325Q channels displayed weaker correlated motions of the S4 and the S4-S5 linker, and the decoupling of the S6 of the pore domain from the VSD, highlighted by the much smaller community in green and the emergence of 2 additional communities colored in pink and gray.

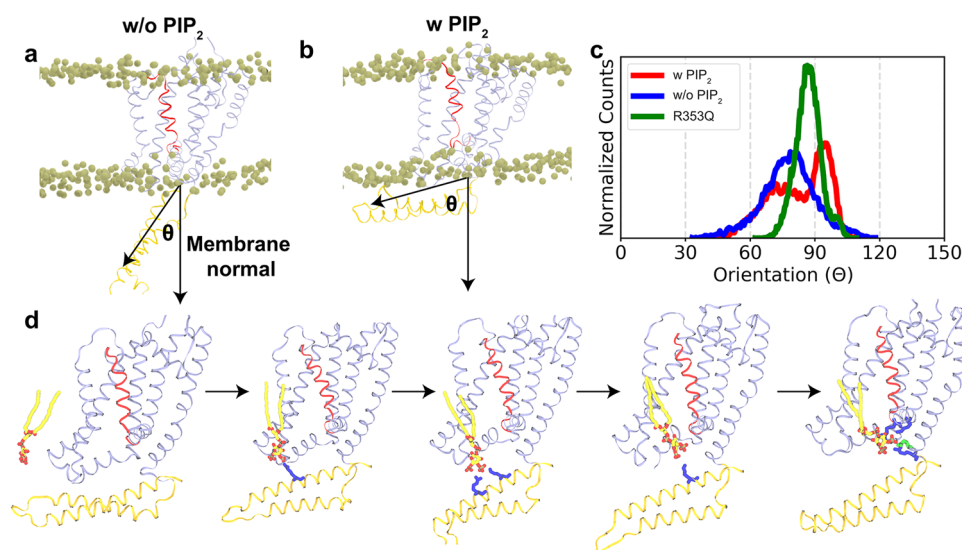


Fig. 7 PIP₂-mediated conformational changes of helices A and B in open K_v7.2 channel. **a** Snapshot of a representative K_v7.2 monomer in PIP₂-free membranes. **b** Snapshot of a representative K_v7.2 monomer in PIP₂-containing membranes. **c** Orientation angle of helices A and B with respect to the membrane normal. The distribution of the orientation angle of helices A and B in WT K_v7.2 channel over the last 200 ns of all the simulations in membranes with (w/) or without (w/o) PIP₂ as well as that of mutant K_v7.2-R353Q channel in membranes with PIP₂. In PIP₂-free membranes, the helical pair of the WT channel adopts a largely solvent-exposed conformation. Addition of PIP₂ induces a drastic conformational change in these helices from a solvent-exposed conformation to a bilayer-interacting conformation. However, the R353Q mutation in the AB linker moves the helices closer to a solvent-exposed conformation even in the presence of PIP₂. **d** Large-scale conformational change in the cytoplasmic helices provides a pathway for PIP₂ movement along Helix-B to its ultimate localization at Site-O4. All the phosphorus atoms of the bilayer are shown in vdW (van der Waals) representation. K_v7.2 protein is shown in ribbon representation with the S4 in red, helices A and B in brown, and the rest of the protein in ice blue.

(Fig. 7), suggesting that PIP₂ binding to R353 contributes to this conformational change.

The conformational change in K_v7.2 is different from that observed in the PIP₂-bound K_v7.1^{22,59} which lacks the analogous arginine residue and shows low sequence homology to the AB linker of K_v7.2. K_v7.3, on the other hand, has the analogous arginine residue in the AB linker with fairly well-conserved sequence, suggesting that K_v7.3 may adopt a similar conformation as K_v7.2 in the presence of PIP₂. We propose that PIP₂ binding to R353 affects the opening of K_v7.2 channels by inducing a bilayer-interacting conformation of the helical pair and facilitating the movement of PIP₂ along Helix-B and its binding to distal Helix-B (Site-O2). Subsequent interaction with other

basic residues in Site-O1 and Site-O4 will induce the transition from the closed to the open state by coordinating allosteric movement of the VSD and the pore domain. R353 is also the target of three epilepsy mutations (ClinVar Database, NCBI)^{60–62}, further supporting the role of R353 in PIP₂ modulation of K_v7.2 channels.

Neuronal K_v7 channels are highly enriched in the axonal surface where they regulate the AP firing threshold, frequency and shape^{13,63}, whereas dendritic K_v7 currents increase the threshold of Ca²⁺ spike initiation⁶⁴. Heterozygous deletion of KCNQ2 gene in mice leads to hippocampal hyperexcitability and increased seizure propensity^{65,66}. Consistent with their critical role in inhibiting neuronal excitability, > 400 BFNE and EE

mutations are found in *KCNQ2*¹⁷. Computational algorithms have identified the S4, the pore loop, the S6, pre-Helix-A, Helix B, and the BC linker as hotspots for EE mutations^{14,67}, whereas BFNE mutations are enriched in the S2-S3 linker⁶⁷. The overlap between epilepsy mutation hotspots and the PIP₂ binding domains identified in our study underscores the critical role of PIP₂ in the pathophysiological mechanism underlying *KCNQ2*-related epilepsy.

Current anti-epileptic drugs are ineffective in treating many epilepsy patients with *K_v7.2* EE variants^{18,19,68}. M-current inhibition upon PIP₂ depletion results in neuronal hyperexcitability⁶⁹, and impaired PIP₂ sensitivity of *K_v7.2* channels is associated with EE variants^{14,25,28}. Retigabine (INN; USAN ezogabine) is a selective agonist of *K_v7.2-K_v7.5* channels, but not *K_v7.1* channel^{70,71}. Retigabine suppresses seizures in animal models and humans^{70,71}, however, it has been discontinued as an anti-epileptic drug due to adverse side effects⁷². However, it may be effective in opening EE mutant channels with impaired PIP₂ binding because it stabilizes the open state of *K_v7.2* and *K_v7.3* channels by binding to a hydrophobic pocket near the gate⁷³. Alternatively, strengthening PIP₂-*K_v7.2* interaction may increase *K_v7* current. For example, zinc pyrithione can rescue M-current in hippocampal neurons following PIP₂ depletion by competing with PIP₂ for *K_v7.2* activation⁷⁴. Recently, a compound, CP1, is shown to substitute PIP₂ for the VSD-pore coupling in *K_v7.1* channel, and to a less extent, *K_v7.2* and *K_v7.2/K_v7.3* channels⁷⁵, suggesting its potential to inhibit neuronal hyperexcitability. Our in-depth investigation of PIP₂-*K_v7.2* interaction may provide the foundation to explore a new class of therapeutics for epilepsy that can control PIP₂ modulation of neuronal *K_v7* channels.

Methods

Structural models of open and closed states of *K_v7.2*. The open and closed conformations of *K_v7.2* channel used in the molecular dynamics (MD) simulations were modeled following the procedure described in a recent study¹⁴. Briefly, the closed conformation of the channel was modeled based on the cryo-EM structure of *K_v7.1* (PDB ID: 5VMS)¹⁰. Multiple sequence alignment of the target template and *K_v7.2* was performed using Toffee web server (<https://www.ebi.ac.uk/Tools/msa/tcoffee/>). After the alignment, the homology model of the closed state was built with MODELLER⁷⁶. Our final model contains residues from 74–363 and 537–594. The open conformation of *K_v7.2* was then constructed by performing non-equilibrium, driven MD simulations. We performed a 20-ns targeted MD (TMD)⁷⁷ simulation during which the closed structure was driven towards an open form, while embedded in a lipid bilayer containing 1-palmitoyl-2-oleoyl-*sn*-glycero-3-phosphatidylcholine (POPC) and 2.2% 1-palmitoyl-2-oleoyl-*sn*-glycero-3-phosphatidylinositol 4,5-bisphosphate (PIP₂) lipids. The target of the TMD simulation was selected to be the highly homologous *K_v1.2/K_v2.1* channel in an open-state conformation (PDB ID: 2R9R)⁷⁸. As major structural changes occur in the pore region of the channel, we applied a restraint ($k = 250$ kcal/mol/Å²; only Ca atoms were driven) on the S4-S5 and S6 helices of each monomer to drive it towards the target open state. The structural stability of the open and closed conformations of *K_v7.2* was evaluated by monitoring the degree of opening of the states, calculated by the number of water molecules in the pore helix and the selectivity filter during 400-ns MD runs in explicit lipid bilayers¹⁴. During these simulations we consistently observed stable and a higher number of water molecules in the open state of the channel, as compared to the closed state¹⁴.

PIP₂-binding simulations. The open and closed conformations of *K_v7.2* were embedded in multiple independently generated POPC membranes with or without 2.2% PIP₂ lipids (Table 1). All the membranes were constructed using the Membrane Builder module in CHARMM-GUI⁷⁹, and the initial placement of PIP₂ lipids was intentionally varied in each membrane. All PIP₂ lipid molecules were initially at least 15 Å away from the protein. The systems were solvated using TIP3P water and buffered at 150 mM KCl to neutralize. The final simulation systems consisted of ~300,000 atoms. All the simulations were performed in the absence of calmodulin. To further examine the specific lipid-protein interactions captured in the modeled closed *K_v7.2*, we also performed additional lipid-binding simulations of a recent cryo-EM structure of *K_v7.2* (PDB ID: 7CR3) after removing calmodulin⁴⁴. All the missing loops were constructed using MODELLER⁷⁶ and the entire tetrameric structure was embedded in an explicit lipid bilayer containing POPC and 2.2% of PIP₂ lipids. Three independent 500-ns simulations were performed on this system.

Molecular dynamics simulation protocols. All the simulations were performed under periodic boundary conditions using NAMD^{80,81} and CHARMM36m force field parameters^{82,83} for protein and lipid. During the initial equilibration, the protein's backbone atoms were harmonically restrained to their initial positions with a force constant of $k = 1$ kcal/mol/Å². The restraints were released at the start of the production run. All the non-bonded forces were calculated with a cutoff of 12 Å and a switching distance of 10 Å. Long-range electrostatic forces were calculated using the particle mesh Ewald (PME) method⁸⁴. A Langevin thermostat using $\gamma = 1$ ps⁻¹ was used to maintain the system temperature at 310 K. The pressure was maintained at 1 bar using a Nosé Hoover Langevin piston method⁸⁵. During pressure control, the simulation box was allowed to fluctuate in all the dimensions with constant ratio in the *xy* (lipid bilayer) plane. An integration time step of 2 fs was used in all the simulations.

Simulation analysis. To characterize lipid-protein interactions and potential lipid binding sites, occupancy maps of the PIP₂ headgroup were calculated using the VOLMAP plugin in VMD⁸⁶. Based on our previous experience³⁵, a 4-Å heavy-atom distance cutoff was chosen to define contacts between the phosphate groups of PIP₂ lipids and protein residues, while a 3.5-Å cutoff was used to define contacts with the hydroxyl groups of PIP₂. The role of PIP₂ lipids in stabilizing the open conformation of *K_v7.2* was determined by performing dynamical network analysis using the NETWORK-VIEW plugin⁸⁷ in VMD. In a network, all Ca atoms are defined as nodes connected by edges if they are within 4.5 Å of each other for at least 75% of the MD trajectory. Pearson correlation was used to define the communities (the set of residues that move in concert) in the network.

DNA construct and mutagenesis. Plasmid pcDNA3 carrying *KCNQ2* cDNA (GenBank: Y15065.1) encoding *K_v7.2* (GenBank: CAA 75348.1) was previously described^{14,25,88,89}. This short isoform of *K_v7.2* lacks 2 exons compared to the reference *K_v7.2* sequence (GenBank: NP_742105.1). Our lab has previously shown that currents through this *K_v7.2* variant can be potentiated by PIP₂ increase and are sensitive to Dr-VSP activation^{14,25}. Plasmid pIRES-dsRed-PIP₂90⁹⁰ was a kind gift from Dr. Anastasios Tzingounis (University of Connecticut). Selected mutations (R214Q, K219N, R325Q, R353Q, R214Q/K219N double mutation, R214Q/K219N/R353Q triple mutation) were generated using the Quik Change II XL Site-Directed Mutagenesis Kit (Agilent) and verified by sequencing the entire cDNA construct. The following primers were used for mutagenesis: R214Q (sense-^{5'}GAT CCG CAT GGA CCG GCA GGG AGG CAC CTG G^{3'}, antisense-^{5'}CCA GGT GCC TCC CTG CCG GTC CAT GCG GAT C^{3'}), K219N (sense-^{5'}GGA GGC ACC TGG AAC CTG CTG GGC TCT GTG^{3'}, antisense-^{5'}CAC AGA GCC CAG CAG GTT CCA GGT GCC TCC^{3'}), R325Q (sense-^{5'}GGT TCA GGA GCA GCA CCA GCA GAA GCA CTT TGA GAA G^{3'}, antisense-^{5'}CTT CTC AAA GTG CTT CTG CTG GTG CTG CTG CTG AAC C^{3'}), R353Q (sense-^{5'}GCC AAC CAC CTC TCG CAG ACA GAC CTG CAC TCC^{3'}, antisense-^{5'}GGA GTG CAG GTC TGT CTG CGA GAG GTT GGT GGC^{3'}).

Electrophysiology. Whole cell patch clamp recording was performed in Chinese ovary cells (CHO hm1) at room temperature (22–24 °C) as described^{14,25}. Cells were plated on 12 mm glass coverslips (Warner Instrument, 1 × 10⁵ cells per coverslip) treated with poly D-lysine (0.1 mg/mL) (Sigma-Aldrich). To express *K_v7.2* channels and PIP5K, cells were transfected with pEGFPN1 (0.2 µg), pIRES-dsRed-PIP₂90 (0.45 µg) and pcDNA3-*K_v7.2* WT or mutant (0.45 µg). For the control experiment of PIP5K, cells were transfected with pEGFPN1 (0.65 µg) and pcDNA3-*K_v7.2* WT or mutant (0.45 µg). At 24–48 h post-transfection, GFP-positive cells were recorded in extracellular solution containing (mM): 138 NaCl, 5.4 KCl, 2 CaCl₂, 1 MgCl₂, 10 D-glucose, and 10 HEPES (pH 7.4, 307–312 mOsm). Patch pipettes (3–4 MΩ) were filled with intracellular solution containing (mM): 140 KCl, 2 MgCl₂, 10 EGTA, 10 HEPES, 5 Mg-ATP (pH 7.4 with KOH, 290–300 mOsm). To record K⁺ currents, cells were held at –80 mV. Currents were evoked by depolarization for 1.5 s from –100 mV to +20 mV in 10-mV increments, followed by a step to 0 mV for 300 ms. Leak-subtracted current densities (pA/pF), normalized conductance and channel biophysical properties were calculated as described²⁵. Briefly, leak current was defined as non-voltage-dependent current through GFP-transfected CHO hm1 cells. Current density was calculated by dividing leak-subtracted current (pA) by capacitance (pF). $V_{1/2}$ and the slope factor (k) were calculated by fitting the points of G/G_{\max} to a Boltzmann equation in the following form: $G/G_{\max} = 1/(1 + \exp(V_{1/2} - V)/k)$.

To examine the decline of *K_v7.2* current upon activation of Dr-VSP, CHO hm1 cells were transfected with pDrVSP-IRES2-EGFP (0.5 µg) and pcDNA3-*K_v7.2* WT or mutant (0.5 µg). The pDrVSP-IRES2-EGFP plasmid was a gift from Yasushi Okamura (Addgene plasmid # 80333). Voltage-clamp recording of *K_v7.2* current upon depolarization-induced Dr-VSP activation was performed as described⁹¹ with an external solution containing 144 mM NaCl, 5 mM KCl, 2 mM CaCl₂, 0.5 mM MgCl₂, 10 mM glucose and 10 mM HEPES (pH 7.4). Patch pipettes (3–4 MΩ) were filled with intracellular solution containing 135 mM potassium aspartate, 2 mM MgCl₂, 1 mM EGTA, 0.1 mM CaCl₂, 4 mM ATP, 0.1 mM GTP and 10 mM HEPES (pH 7.2). Cells were held at –70 mV and 10 s step depolarizations were applied in 20-mV steps from –20 to +100 mV with 2 min inter-step intervals to allow PIP₂ regeneration. The extent of *K_v7.2* current decay upon Dr-VSP activation during

10 s depolarization was measured as the ratio of current at 10 s over peak current at each voltage step.

Western blot. CHO hm1 cells were plated on 35 mm tissue culture dishes (Corning, 3×10^5 cells per well). Next day, cells were transfected with pcDNA3-K_v7.2 WT or mutant (0.5 µg) using FuGENE6 transfection reagent (Promega). At 24 h post-transfection, cells were lysed, and lysates were analyzed by immunoblotting as described¹⁴. Briefly, cells were collected by cell scraper in 300 µL ice-cold lysis buffer containing (mM): 150 NaCl, 50 Tris, 2 EGTA, 1 EDTA, 1% Triton-X, 0.5% deoxycholic acid (pH 7.4), supplemented with Halt protease inhibitor cocktail (Thermo Fisher Scientific). Lysates were harvested by 15 min incubation on ice, followed by 15 min centrifugation at $14,000 \times g$ in 4 °C. Samples were mixed with SDS sample buffer in 1:5 ratio and heated at 75 °C for 30 min. The SDS sample buffer contained (mM): 75 Tris, 50 TCEP, 0.5 EDTA, 10% SDS, 12.5% glycerol, 0.5 mg/mL Bromophenol Blue. The samples were then run on 4%–20% gradient SDS-PAGE gels (Bio-Rad) and transferred to a methanol-treated polyvinylidene difluoride (PVDF) membrane (Millipore). The membranes were blocked with blocking buffer (5% nonfat milk/0.1% Tween-20 in Tris-buffered saline/TBS containing 150 mM NaCl, 50 mM Tris, pH 7.5) for 1 h followed by overnight incubation of primary antibodies in washing buffer (1% nonfat milk/0.1% Tween-20 in TBS) in 4 °C. After 1 hr incubation with horse radish peroxidase (HRP)-conjugated secondary antibodies in washing buffer, membranes were treated with Enhanced Chemiluminescence substrate (ECL, Thermo Fisher Scientific, #32106) and immediately imaged with the iBright CL1000 imaging system (Thermo Fisher Scientific). Acquired images were analyzed using ImageJ software (National Institutes of Health). GAPDH, α-tubulin and β-tubulin were used as loading controls. Background-subtracted intensities of each immunoblot band was measured and the K_v7.2/loading control ratio of WT or mutants was computed. The K_v7.2/loading control of WT was used as 100% and mutants were normalized to WT as described¹⁴. Antibodies used include anti-GAPDH (Cell Signaling #2118, 1:1000 dilution), anti-α-tubulin (Cell Signaling #2144, 1:1000 dilution), anti-β-tubulin (Cell Signaling #2146, 1:1000), anti-K_v7.2 (Neuromab, N26A/23, 1:200 dilution), donkey anti-rabbit and donkey anti-mouse HRP secondary antibodies (The Jackson Laboratory, 711-035-152; 715-035-150).

Surface biotinylation. CHO hm1 cells were plated on 60 mm culture dishes (Corning, 8×10^5 cells per well). Next day, cells were transfected with pcDNA3-K_v7.2 WT or mutant (0.8 µg) using FuGENE6 transfection reagent (Promega). At 24 h post-transfection, the cells were subjected to surface biotinylation as previously described⁹². The culture dishes containing transfected cells were placed on ice and washed with 1X PBS twice. To biotinylate surface proteins, the cells were then incubated with Sulfo-NHS-SS-Biotin (1 mg/mL, Pierce) in ice-cold PBS (3 mL) for 20 min. The cells were then washed with 1X PBS twice and 1X TBS once. Cells were collected using cell scraper in 400 µL ice-cold lysis buffer containing: (mM): 150 NaCl, 50 Tris, 2 EGTA, 1 EDTA, 1% Triton-X, 0.5% deoxycholic acid, supplemented with Halt protease inhibitor cocktail (Thermo Fisher Scientific). Lysates were harvested by 15 min incubation on ice, followed by 15 min centrifugation at $14,000 \times g$ at 4 °C. 40 µL lysates were saved for western blotting. The remaining 360 µL of lysates were incubated with 50% NeutraAvidin agarose beads (Pierce, 100 µL of 1:1 slurry) for overnight at 4 °C to isolate biotinylated surface proteins from the lysate. After washing with the lysis buffer, biotinylated surface proteins were eluted by heating in 1x SDS sample buffer containing 50 mM TCEP at 75 °C for 30 min. Eluted biotinylated surface proteins and lysates were examined by immunoblotting for K_v7.2 and α-tubulin or β-tubulin as described in the previous section. ImageJ software (NIH) was used to measure background-subtracted intensity of each immunoblot band, and surface or total K_v7.2 intensity was normalized to total α-tubulin or β-tubulin band intensity. To confirm that cell membranes were intact and intracellular proteins were not biotinylated during surface biotinylation, immunoblot of biotinylated surface proteins was also performed with anti-α-tubulin or anti-β-tubulin.

Statistics and reproducibility. All the measurements were taken from distinct samples. All electrophysiology and immunoblotting data are reported as mean ± SEM. Origin 9.1 (OriginLab, Inc) was used for Student's *t*-test and one-way ANOVA with post-hoc Fisher's multiple comparison tests. Specifically, one-way ANOVA with post-hoc Fisher's test was used for surface biotinylation and electrophysiology figures with the exception that Student's unpaired *t*-test was used when comparing the results before and after PIP5K cotransfection in Supplementary Fig. 4a–b. Listed sample sizes of electrophysiology indicate number of cells successfully recorded, while the sample sizes of surface biotinylation studies represent the numbers of experimental replica. Statistical significance was assessed at a priori value (*p*) < 0.05.

Reporting summary. Further information on research design is available in the Nature Research Reporting Summary linked to this article.

Data availability

The datasets generated and analyzed in the current study and presented as the main and supplementary figures are available in the Figshare repository with the identifier

<https://doi.org/10.6084/m9.figshare.15181038>⁹³. All other data that support the findings of this study will be available from the corresponding authors upon reasonable request.

Code availability

Simulation trajectories were collected using the simulation program NAMD. Visualization and analysis were performed using VMD and Python. All of these software packages are publicly available.

Received: 17 August 2020; Accepted: 23 September 2021;

Published online: 14 October 2021

References

- Di Paolo, G. & De Camilli, P. Phosphoinositides in cell regulation and membrane dynamics. *Nature* **443**, 651–657 (2006).
- Suh, B. C. & Hille, B. PIP2 is a necessary cofactor for ion channel function: how and why? *Annu. Rev. Biophys.* **37**, 175–195 (2008).
- Zaydman, M. A. & Cui, J. PIP2 regulation of KCNQ channels: biophysical and molecular mechanisms for lipid modulation of voltage-dependent gating. *Front. Physiol.* **5**, 195 (2014).
- Huang, C. L., Feng, S. & Hilgemann, D. W. Direct activation of inward rectifier potassium channels by PIP2 and its stabilization by Gbetagamma. *Nature* **391**, 803–806 (1998).
- Rodriguez-Menchaca, A. A., Adney, S. K., Zhou, L. & Logothetis, D. E. Dual regulation of voltage-sensitive ion channels by PIP(2). *Front. Pharm.* **3**, 170 (2012).
- Zhang, H. et al. PIP(2) activates KCNQ channels, and its hydrolysis underlies receptor-mediated inhibition of M currents. *Neuron* **37**, 963–975 (2003).
- Maljevic, S., Wuttke, T. V., Seeböhm, G. & Lerche, H. KV7 channelopathies. *Pflug. Arch.* **460**, 277–288 (2010).
- Robbins, J. KCNQ potassium channels: physiology, pathophysiology, and pharmacology. *Pharm. Ther.* **90**, 1–19 (2001).
- Cui, J. Voltage-dependent gating: novel insights from KCNQ1 channels. *Biophys. J.* **110**, 14–25 (2016).
- Sun, J. & MacKinnon, R. Cryo-EM structure of a KCNQ1/CaM complex reveals insights into congenital long QT syndrome. *Cell* **169**, 1042–1050 e1049 (2017).
- Haitin, Y. & Attali, B. The C-terminus of Kv7 channels: a multifunctional module. *J. Physiol.* **586**, 1803–1810 (2008).
- Greene, D. L. & Hoshi, N. Modulation of Kv7 channels and excitability in the brain. *Cell Mol. Life Sci.* **74**, 495–508 (2017).
- Brown, D. A. & Passmore, G. M. Neural KCNQ (Kv7) channels. *Br. J. Pharm.* **156**, 1185–1195 (2009).
- Zhang, J. et al. Identifying mutation hotspots reveals pathogenetic mechanisms of KCNQ2 epileptic encephalopathy. *Sci. Rep.* **10**, 4756 (2020).
- Lehman, A. et al. Loss-of-function and gain-of-function mutations in KCNQ5 cause intellectual disability or epileptic encephalopathy. *Am. J. Hum. Genet.* **101**, 65–74 (2017).
- Charlier, C. et al. A pore mutation in a novel KQT-like potassium channel gene in an idiopathic epilepsy family. *Nat. Genet.* **18**, 53–55 (1998).
- Miceli, F. et al. in GeneReviews(R) (eds M. P. Adam et al.) (1993).
- Weckhuysen, S. et al. KCNQ2 encephalopathy: emerging phenotype of a neonatal epileptic encephalopathy. *Ann. Neurol.* **71**, 15–25 (2012).
- Millichap, J. J. et al. KCNQ2 encephalopathy: Features, mutational hot spots, and ezogabine treatment of 11 patients. *Neurol. Genet.* **2**, e96 (2016).
- Suh, B. C. & Hille, B. Recovery from muscarinic modulation of M current channels requires phosphatidylinositol 4,5-bisphosphate synthesis. *Neuron* **35**, 507–520 (2002).
- Zaydman, M. A. et al. Kv7.1 ion channels require a lipid to couple voltage sensing to pore opening. *Proc. Natl Acad. Sci. USA* **110**, 13180–13185 (2013).
- Sun, J. & MacKinnon, R. Structural basis of human KCNQ1 modulation and gating. *Cell* **180**, 340–347 e349 (2020).
- Tobelaïm, W. S. et al. Competition of calcified calmodulin N lobe and PIP2 to an LQT mutation site in Kv7.1 channel. *Proc. Natl Acad. Sci. USA* **114**, E869–E878 (2017).
- Li, Y. et al. KCNE1 enhances phosphatidylinositol 4,5-bisphosphate (PIP2) sensitivity of IKs to modulate channel activity. *Proc. Natl Acad. Sci. USA* **108**, 9095–9100 (2011).
- Kim, E. C. et al. Reduced axonal surface expression and phosphoinositide sensitivity in Kv7 channels disrupts their function to inhibit neuronal excitability in Kcnq2 epileptic encephalopathy. *Neurobiol. Dis.* **118**, 76–93 (2018).
- Hernandez, C. C., Zaika, O. & Shapiro, M. S. A carboxy-terminal inter-helix linker as the site of phosphatidylinositol 4,5-bisphosphate action on Kv7 (M-type) K⁺ channels. *J. Gen. Physiol.* **132**, 361–381 (2008).

27. Choveau, F. S., De la Rosa, V., Bierbower, S. M., Hernandez, C. C. & Shapiro, M. S. Phosphatidylinositol 4,5-bisphosphate (PIP₂) regulates KCNQ3 K(+) channels by interacting with four cytoplasmic channel domains. *J. Biol. Chem.* **293**, 19411–19428 (2018).
28. Soldovieri, M. V. et al. Early-onset epileptic encephalopathy caused by a reduced sensitivity of Kv7.2 potassium channels to phosphatidylinositol 4,5-bisphosphate. *Sci. Rep.* **6**, 38167 (2016).
29. Ambrosino, P. et al. Kv7.3 compound heterozygous variants in early onset encephalopathy reveal additive contribution of C-terminal residues to PIP₂-dependent K(+) channel gating. *Mol. Neurobiol.* **55**, 7009–7024 (2018).
30. Muller, M. P. et al. Characterization of lipid-protein interactions and lipid-mediated modulation of membrane protein function through molecular simulation. *Chem. Rev.* **119**, 6086–6161 (2019).
31. Duncan, A. L., Corey, R. A. & Sansom, M. S. P. Defining how multiple lipid species interact with inward rectifier potassium (Kir2) channels. *Proc. Natl Acad. Sci. USA* **117**, 7803–7813 (2020).
32. Soubias, O. et al. Membrane surface recognition by the ASAP1 PH domain and consequences for interactions with the small GTPase Arf1. *Sci. Adv.* **6**, <https://doi.org/10.1126/sciadv.abd1882> (2020).
33. Miranda, W. E. et al. Lipid regulation of hERG1 channel function. *Nat. Commun.* **12**, 1409 (2021).
34. Kasimova, M. A., Tarek, M., Shaytan, A. K., Shaitan, K. V. & Delemotte, L. Voltage-gated ion channel modulation by lipids: insights from molecular dynamics simulations. *Biochim. Biophys. Acta* **1838**, 1322–1331 (2014).
35. Yu, K., Jiang, T., Cui, Y., Tajkhorshid, E. & Hartzell, H. C. A network of phosphatidylinositol 4,5-bisphosphate binding sites regulates gating of the Ca(2+) -activated Cl(-) channel ANO1 (TMEM16A). *Proc. Natl Acad. Sci. USA* **116**, 19952–19962 (2019).
36. Schwake, M., Pusch, M., Kharkovets, T. & Jentsch, T. J. Surface expression and single channel properties of KCNQ2/KCNQ3, M-type K+ channels involved in epilepsy. *J. Biol. Chem.* **275**, 13343–13348 (2000).
37. Wang, H. S. et al. KCNQ2 and KCNQ3 potassium channel subunits: molecular correlates of the M-channel. *Science* **282**, 1890–1893 (1998).
38. Etxeberria, A., Santana-Castro, I., Regalado, M. P., Aivar, P. & Villarreal, A. Three mechanisms underlie KCNQ2/3 heteromeric potassium M-channel potentiation. *J. Neurosci.* **24**, 9146–9152 (2004).
39. Zaika, O., Hernandez, C. C., Bal, M., Tolstykh, G. P. & Shapiro, M. S. Determinants within the turret and pore-loop domains of KCNQ3 K+ channels governing functional activity. *Biophys. J.* **95**, 5121–5137 (2008).
40. Soh, H., Pant, R., LoTurco, J. J. & Tzingounis, A. V. Conditional deletions of epilepsy-associated KCNQ2 and KCNQ3 channels from cerebral cortex cause differential effects on neuronal excitability. *J. Neurosci.* **34**, 5311–5321 (2014).
41. Soldovieri, M. V., Miceli, F. & Tagliatela, M. Driving with no brakes: molecular pathophysiology of Kv7 potassium channels. *Physiol. (Bethesda)* **26**, 365–376 (2011).
42. Nappi, P. et al. Epileptic channelopathies caused by neuronal Kv7 (KCNQ) channel dysfunction. *Pflug. Arch.* **472**, 881–898 (2020).
43. Gomis-Perez, C. et al. Homomeric Kv7.2 current suppression is a common feature in KCNQ2 epileptic encephalopathy. *Epilepsia* **60**, 139–148 (2019).
44. Li, X. et al. Molecular basis for ligand activation of the human KCNQ2 channel. *Cell Res.* **31**, 52–61 (2021).
45. Kosenko, A. et al. Coordinated signal integration at the M-type potassium channel upon muscarinic stimulation. *EMBO J.* **31**, 3147–3156 (2012).
46. Gamper, N., Stockand, J. D. & Shapiro, M. S. The use of Chinese hamster ovary (CHO) cells in the study of ion channels. *J. Pharm. Toxicol. Methods* **51**, 177–185 (2005).
47. van den Bout, I. & Divecha, N. PIP5K-driven PtdIns(4,5)P₂ synthesis: regulation and cellular functions. *J. Cell Sci.* **122**, 3837–3850 (2009).
48. Li, Y., Gamper, N., Hilgemann, D. W. & Shapiro, M. S. Regulation of Kv7 (KCNQ) K+ channel open probability by phosphatidylinositol 4,5-bisphosphate. *J. Neurosci.* **25**, 9825–9835 (2005).
49. Jensen, M. O. et al. Mechanism of voltage gating in potassium channels. *Science* **336**, 229–233 (2012).
50. Zhang, Q. et al. Dynamic PIP₂ interactions with voltage sensor elements contribute to KCNQ2 channel gating. *Proc. Natl Acad. Sci. USA* **110**, 20093–20098 (2013).
51. Pisano, T. et al. Early and effective treatment of KCNQ2 encephalopathy. *Epilepsia* **56**, 685–691 (2015).
52. Kim, R. Y., Pless, S. A. & Kurata, H. T. PIP₂ mediates functional coupling and pharmacology of neuronal KCNQ channels. *Proc. Natl Acad. Sci. USA* **114**, E9702–E9711 (2017).
53. Fang, Z. X. et al. KCNQ2 related early-onset epileptic encephalopathies in Chinese children. *J. Neurol.* **266**, 2224–2232 (2019).
54. Miraglia del Giudice, E. et al. Benign familial neonatal convulsions (BFNC) resulting from mutation of the KCNQ2 voltage sensor. *Eur. J. Hum. Genet.* **8**, 994–997 (2000).
55. Castaldo, P. et al. Benign familial neonatal convulsions caused by altered gating of KCNQ2/KCNQ3 potassium channels. *J. Neurosci.* **22**, RC199 (2002).
56. Hou, P. et al. Two-stage electro-mechanical coupling of a KV channel in voltage-dependent activation. *Nat. Commun.* **11**, 676 (2020).
57. Slesinger, P. A. & Wickman, K. *Structure to Function of G Protein-Gated Inwardly Rectifying (GIRK) Channels*. 1 edn, Vol. 123 (Academic Press, 2015).
58. Eckey, K. et al. Novel Kv7.1-phosphatidylinositol 4,5-bisphosphate interaction sites uncovered by charge neutralization scanning. *J. Biol. Chem.* **289**, 22749–22758 (2014).
59. Kang, P. W. et al. Calmodulin acts as a state-dependent switch to control a cardiac potassium channel opening. *Sci. Adv.* **6**, <https://doi.org/10.1126/sciadv.abd6798> (2020).
60. Milh, M. et al. Variable clinical expression in patients with mosaicism for KCNQ2 mutations. *Am. J. Med. Genet. A* **167A**, 2314–2318 (2015).
61. Richards, M. C. et al. Novel mutations in the KCNQ2 gene link epilepsy to a dysfunction of the KCNQ2-calmodulin interaction. *J. Med. Genet.* **41**, e35 (2004).
62. Sands, T. T. et al. Rapid and safe response to low-dose carbamazepine in neonatal epilepsy. *Epilepsia* **57**, 2019–2030 (2016).
63. Shah, M. M., Migliore, M., Valencia, I., Cooper, E. C. & Brown, D. A. Functional significance of axonal Kv7 channels in hippocampal pyramidal neurons. *Proc. Natl Acad. Sci. USA* **105**, 7869–7874 (2008).
64. Yue, C. & Yaari, Y. Axo-somatic and apical dendritic Kv7/M channels differentially regulate the intrinsic excitability of adult rat CA1 pyramidal cells. *J. Neurophysiol.* **95**, 3480–3495 (2006).
65. Kim, E. C. et al. Heterozygous loss of epilepsy gene KCNQ2 alters social, repetitive and exploratory behaviors. *Genes Brain Behav.* **19**, e12599 (2020).
66. Watanabe, H. et al. Disruption of the epilepsy KCNQ2 gene results in neural hyperexcitability. *J. Neurochem.* **75**, 28–33 (2000).
67. Goto, A. et al. Characteristics of KCNQ2 variants causing either benign neonatal epilepsy or developmental and epileptic encephalopathy. *Epilepsia* **60**, 1870–1880 (2019).
68. Numis, A. L. et al. KCNQ2 encephalopathy: delineation of the electroclinical phenotype and treatment response. *Neurology* **82**, 368–370 (2014).
69. Delmas, P. & Brown, D. A. Pathways modulating neural KCNQ/M (Kv7) potassium channels. *Nat. Rev. Neurosci.* **6**, 850–862 (2005).
70. Blackburn-Munro, G., Dalby-Brown, W., Mirza, N. R., Mikkelsen, J. D. & Blackburn-Munro, R. E. Retigabine: chemical synthesis to clinical application. *CNS Drug Rev.* **11**, 1–20 (2005).
71. Gunthorpe, M. J., Large, C. H. & Sankar, R. The mechanism of action of retigabine (ezogabine), a first-in-class K+ channel opener for the treatment of epilepsy. *Epilepsia* **53**, 412–424 (2012).
72. Mathias, S. V. & Abou-Khalil, B. W. Ezogabine skin discoloration is reversible after discontinuation. *Epilepsy Behav. Case Rep.* **7**, 61–63 (2017).
73. Kim, R. Y. et al. Atomic basis for therapeutic activation of neuronal potassium channels. *Nat. Commun.* **6**, 8116 (2015).
74. Zhou, P. et al. Phosphatidylinositol 4,5-bisphosphate alters pharmacological selectivity for epilepsy-causing KCNQ potassium channels. *Proc. Natl Acad. Sci. USA* **110**, 8726–8731 (2013).
75. Liu, Y. et al. A PIP₂ substitute mediates voltage sensor-pore coupling in KCNQ activation. *Commun. Biol.* **3**, 385 (2020).
76. Webb, B. & Sali, A. Comparative Protein Structure Modeling Using MODELLER. *Curr. Protoc. Bioinforma.* **54**, 5 6 1–5 6 37 (2016).
77. Schlitter, J., Engels, M., Krüger, P., Jacoby, E. & Wollmer, A. Targeted molecular dynamics simulation of conformational change-application to the T ↔ R transition in insulin. *Mol. Simul.* **10**, 291–308 (1993).
78. Long, S. B., Tao, X., Campbell, E. B. & MacKinnon, R. Atomic structure of a voltage-dependent K+ channel in a lipid membrane-like environment. *Nature* **450**, 376–382 (2007).
79. Jo, S., Kim, T., Iyer, V. G. & Im, W. CHARMM-GUI: a web-based graphical user interface for CHARMM. *J. Comput. Chem.* **29**, 1859–1865 (2008).
80. Phillips, J. C. et al. Scalable molecular dynamics with NAMD. *J. Comput. Chem.* **26**, 1781–1802 (2005).
81. Phillips, J. C. et al. Scalable molecular dynamics on CPU and GPU architectures with NAMD. *J. Chem. Phys.* **153**, 044130 (2020).
82. Best, R. B. et al. Optimization of the additive CHARMM all-atom protein force field targeting improved sampling of the backbone phi, psi and side-chain chi(1) and chi(2) dihedral angles. *J. Chem. Theory Comput.* **8**, 3257–3273 (2012).
83. Klauda, J. B. et al. Update of the CHARMM all-atom additive force field for lipids: validation on six lipid types. *J. Phys. Chem. B* **114**, 7830–7843 (2010).
84. Essmann, U. et al. A smooth particle mesh Ewald method. *J. Chem. Phys.* **103**, 8577–8593 (1995).
85. Martyna, G. J., Tobias, D. J. & Klein, M. L. Constant pressure molecular dynamics algorithms. *J. Chem. Phys.* **101**, 4177–4189 (1994).
86. Humphrey, W., Dalke, A. & Schulten, K. VMD: visual molecular dynamics. *J. Mol. Graph.* **14**(33–38), 27–38 (1996).
87. Sethi, A., Eargle, J., Black, A. A. & Luthey-Schulten, Z. Dynamical networks in tRNA:protein complexes. *Proc. Natl Acad. Sci. USA* **106**, 6620–6625 (2009).
88. Cavaretta, J. P. et al. Polarized axonal surface expression of neuronal KCNQ potassium channels is regulated by calmodulin interaction with KCNQ2 subunit. *PLoS ONE* **9**, e103655 (2014).

89. Chung, H. J., Jan, Y. N. & Jan, L. Y. Polarized axonal surface expression of neuronal KCNQ channels is mediated by multiple signals in the KCNQ2 and KCNQ3 C-terminal domains. *Proc. Natl Acad. Sci. USA* **103**, 8870–8875 (2006).
90. Kim, K. S., Duignan, K. M., Hawryluk, J. M., Soh, H. & Tzingounis, A. V. The voltage activation of cortical KCNQ channels depends on global PIP2 levels. *Biophys. J.* **110**, 1089–1098 (2016).
91. Kosenko, A. & Hoshi, N. A change in configuration of the calmodulin-KCNQ channel complex underlies Ca²⁺-dependent modulation of KCNQ channel activity. *PLoS ONE* **8**, e82290 (2013).
92. Baculis, B. C. et al. Prolonged seizure activity causes caspase dependent cleavage and dysfunction of G-protein activated inwardly rectifying potassium channels. *Sci. Rep.* **7**, 12313 (2017).
93. Pant, S. et al. MD simulation and electrophysiological characterization of PIP2-binding residues in Kv7.2 channel Datasets. figshare <https://doi.org/10.6084/m9.figshare.15181038> (2021)

Acknowledgements

This research was supported by the National Institutes of Health under awards R01-GM123455 and P41-GM104601 from the National Institute of General Medical Sciences (to E.T.) and R01-NS083402 and R01-NS097610 from the National Institute of Neurological Disorders and Stroke (to H.J.C.). S.P. acknowledges receiving support from the Beckman Institute Graduate Fellowship. We would like to also acknowledge the computing resources provided by Blue Waters of National Center for Supercomputing Applications (to E.T.) and by Extreme Science and Engineering Discovery Environment (XSEDE award MCA06N060 to E.T.) and TACC Frontera. We would like to thank Tao Jiang for her assistance with simulations on Frontera. All authors declare no competing interests.

Author contributions

S.P., J.Z., H.J.C. and E.T. conceived of the study and participated in its design and coordination. S.P., K.L. and E.T. performed and analyzed MD simulation. E.C.K., J.Z. and H.J.C. generated and characterized selected mutations. S.P., J.Z., E.C.K., H.J.C. and E.T. wrote the manuscript. All authors read and approved the final manuscript.

Competing interests

The authors declare no competing interests.

Additional information

Supplementary information The online version contains supplementary material available at <https://doi.org/10.1038/s42003-021-02729-3>.

Correspondence and requests for materials should be addressed to Hee Jung Chung or Emad Tajkhorshid.

Peer review information *Communications Biology* thanks the anonymous reviewers for their contribution to the peer review of this work. Primary Handling Editors: Anam Akhtar.

Reprints and permission information is available at <http://www.nature.com/reprints>

Publisher's note Springer Nature remains neutral with regard to jurisdictional claims in published maps and institutional affiliations.



Open Access This article is licensed under a Creative Commons Attribution 4.0 International License, which permits use, sharing, adaptation, distribution and reproduction in any medium or format, as long as you give appropriate credit to the original author(s) and the source, provide a link to the Creative Commons license, and indicate if changes were made. The images or other third party material in this article are included in the article's Creative Commons license, unless indicated otherwise in a credit line to the material. If material is not included in the article's Creative Commons license and your intended use is not permitted by statutory regulation or exceeds the permitted use, you will need to obtain permission directly from the copyright holder. To view a copy of this license, visit <http://creativecommons.org/licenses/by/4.0/>.

© The Author(s) 2021